The Influence of Electrical Fields on the Microstructural Evolution of Alumina

Asaf Reuven Kazmirsky

The Influence of Electrical Fields on the Microstructural Evolution of Alumina

Research Thesis

In Partial Fulfillment of the

Requirements for the Degree of

Master of Science

in Materials Engineering

Asaf Reuven Kazmirsky

Submitted to the Senate of the Technion-Israel Institute of Technology

Av 5785 Haifa July 2025

The research thesis was done under the supervision of **Prof. Wayne D. Kaplan** in the Department of Materials Science & Engineering at the Technion.

The generous financial support of an Israel Science Foundation Grant (ISF 544/22) is gratefully acknowledged.

The author of this thesis states that the research, including the collection, processing and presentation of data, addressing and comparing to previous research, etc., was done entirely in an honest way, as expected from scientific research that is conducted according to the ethical standards of the academic world. Also, reporting the research and its results in this thesis was done in an honest and complete manner, according to the same standards.

List of Publications:

In Preparation:

1. Asaf Kazmirsky, Rachel Marder, and Wayne D. Kaplan, *The Influence of Electrical Fields and Ca on Grain Growth in Alumina,* 2025.

Table of Contents

List of Figures

List of Tables

Abstract

Grain growth is a process that occurs simultaneously with densification during the sintering of ceramic materials. The grain size and area of GBs play a key role in determining the mechanical and functional properties of polycrystalline materials. As such, understanding grain growth is important when it comes to controlling and engineering the properties of ceramics.

It has been demonstrated that electric fields, which are employed as part of sintering techniques like spark plasma sintering (SPS) and flash sintering, also influence the grain growth kinetics. In the case of α-alumina (α-Al_2O_3), the reason is believed to be the attraction of locally positively charged oxygen vacancies to the negative electrode. Doping alumina with calcium increases the amount of oxygen vacancies to compensate for the charge difference between calcium and aluminum cations.

In this work, the influence of calcium doping and an electric field on grain growth in alumina was studied at 1600°C. Undoped and Ca-doped (6 and 19 ppm of Ca, respectively) alumina samples were placed between electrodes in a tube furnace and annealed with and without an electric field. The effective grain boundary mobility was calculated from average grain size measurements.

It was confirmed that Ca-doping increases the effective grain boundary mobility from $11.3 \cdot 10^{-15}$ m^2/s to $22.9 \cdot 10^{-15}$ (without a field). The grain boundary mobilities measured after applying an electric field of 200 V/cm on the undoped alumina samples were $4.9 \cdot 10^{-15}$ m^2/s near the positive electrode, $10.1 \cdot 10^{-15}$ m^2/s at the middle of the sample and $9.1 \cdot 10^{-15}$ m^2/s near the negative electrode.

When increasing the strength of the field to 300 V/cm, the measured mobilities were $5.0 \cdot 10^{-15}$ m^2/s near positive electrode, $8.3 \cdot 10^{-15}$ m^2/s at the middle of the sample and $12.0 \cdot 10^{-15}$ m^2/s near the negative electrode.

For the Ca-doped alumina annealed under a field of 300 V/cm, the measured mobilities were $8.5 \cdot 10^{-15}$ m^2/s near the positive electrode, $14.3 \cdot 10^{-15}$ m^2/s at the middle of the sample and $22.1 \cdot 10^{-15}$ m^2/s near the negative electrode.

Quantitative wavelength dispersive spectroscopy (WDS) was used to determine that the electric field causes an inhomogeneous distribution of calcium in the sample by measuring the Ca content as a function of distance from the electrodes in the Ca-doped sample annealed for 8 hours. The mobility measured near the positive electrode corresponds to a *higher Ca concentration* (19 ppm), and the mobility measured near the negative electrode corresponds to a *lower Ca concentration* (10 ppm) indicating that oxygen vacancies are responsible for increasing the grain boundary mobility in alumina and that Ca by itself actually causes the traditional solute-drag effect.

List of Abbreviations

DC	Direct current
EDS	Energy dispersive spectroscopy
FIB	Focused ion beam
GB	Grain boundary
ICP	Inductively coupled plasma spectroscopy
ppm	Parts per million
SE	Secondary electrons
SEM	Scanning electron microscopy
SPS	Spark plasma sintering
STEM	Scanning transmission electron microscopy
TEM	Transmission electron microscopy
WDS	Wavelength dispersive spectroscopy
WMC	Weighted mean curvature
XRD	X-ray diffraction

List of Symbols

A	Area of the interface inside the interaction volume
$C_{lim,0.975}$	Limit of detection at confidence probability of 97.5%
C_{std}	Concentration within the standard
C_{∞}	Bulk solute concentration
D	Dry weight
Fz	Zener drag force
F_p	Pore/particle Zener drag force
G	Grain size
ΔG	Change in Gibbs free energy
I_{sample}, I_{std}, I_{bgd}	Measured X-ray intensity from the sample, the standard and the background, respectively
k_1	Rate constant
ΔL	Migration distance
M_{GB}	Grain boundary mobility
M_p	Pore/particle mobility
M_s	Single crystal mobility
N_z	Number of particles/pores
ΔP	Pressure difference
S	Suspended weight
T	Temperature
V	Potential
V_{GB}	Grain boundary velocity
V_p	Pore velocity
W	Saturated weight
α	Geometrical factor for grains geometry
Γ	Surface excess of solute
γ	Surface or interface energy
τ	Single measurement time
θ	Dihedral angle

1. Literature Survey

1.1 Solid State Sintering

When sintering ceramic materials, the goal is to go from a porous green body, made by compacting ceramic powder, to a material as dense as possible. This final processing stage subjects the green body to thermal energy at a temperature roughly around 70% of the material's melting temperature. At these high temperatures, there is sufficient energy for mass transfer (diffusion) to occur, leading to densification. Atoms go from regions of a high chemical potential to those of a lower chemical potential [1]. The mass transfer can occur via several diffusion mechanisms, as is presented and detailed in Figure 1.

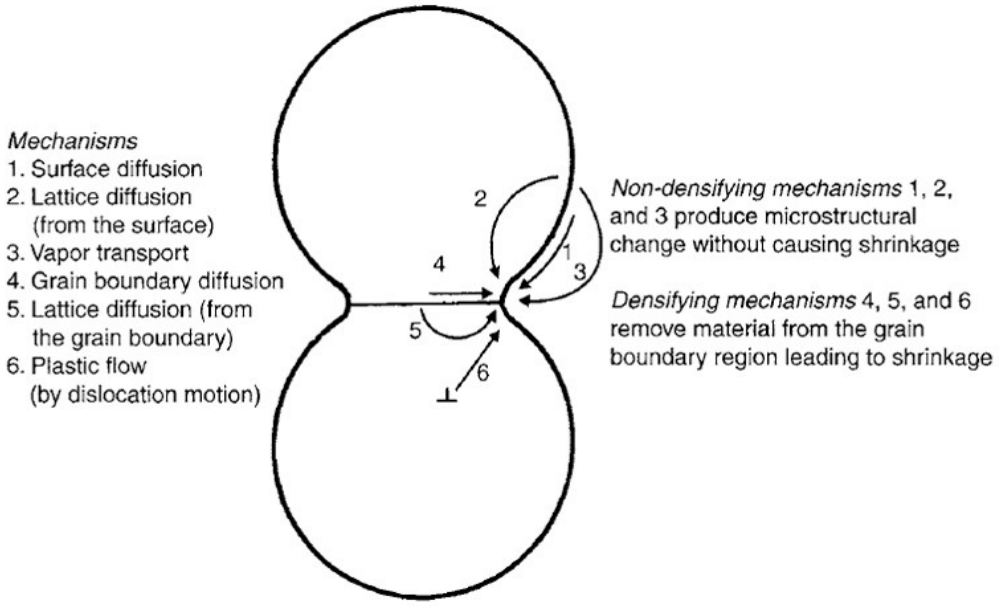

Figure 1: Schematic illustration of diffusion mechanisms during sintering; reproduced from [1].

The driving force for the sintering process is the reduction of the excess surface energy of the system. It can be described as [2]:

$$\Delta(\gamma A) = \Delta\gamma A + \gamma\Delta A \tag{1}$$

where γ is the total surface (interface) energy, A is the total surface area and γA is the total surface/interface energy of the system.

While the aim during sintering is just to achieve densification, two competing phenomena occur simultaneously at these high temperatures, as is depicted in Figure 2.

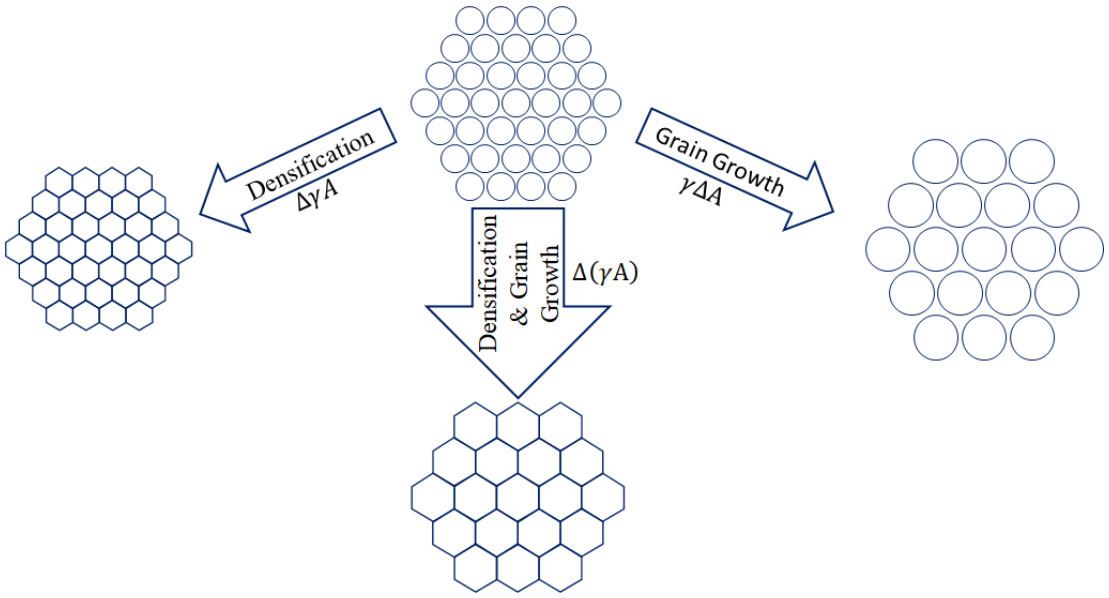

Figure 2: Schematic illustration of densification and grain growth that occur during sintering; redrawn from [2].

The driving force for densification is the reduction of the surface excess energy (Δγ) by replacing the free surfaces of particles with GBs, which generally have a lower excess energy than that of free surfaces. This reduction lowers the overall energy of the system (γA).

The competing process during sintering is grain growth, also known as coarsening. The driving force for grain growth is the reduction of the total grain boundary area (ΔA). Thus, while the specific excess surface energy (γ) remains unchanged, γΔA is lowered, as is the overall energy of the system.

When densification is dominant, the density of the green body increases as the particles coalesce and pores are eliminated. Meanwhile, when coarsening is the dominant process, both the particles and the pores within the ceramic material will increase in size and decrease in number. The larger grains and pores, as well as the overall lower density, can have a negative impact on the material's mechanical properties such as wear resistance, strength, etc. The sintering of most ceramic materials is characterized by a dominant densification effect at the start of the process. As the green bodies continue to densify, grain growth gradually becomes more prominent.

1.2 Grain Growth

1.2.1 Curvature

In order to reduce the grain boundary area and lower the excess energy of the system, the GBs (GBs) migrate. This process involves the short-range motion of atoms from the smaller, shrinking grain to the larger, expanding one, in the direction opposite to that in which the GB moves (as is depicted in Figure 3). The driving force for this reorientation of atoms from one side of the GB to the other is typically described using the curvature of the GB. It is believed to induce a difference in the chemical potential between the two grains because of the variation in pressure between them, causing the chemical potential of the convex grains to be higher than that of the concave grains.

The variation in pressure be described as:

$$\Delta P = \gamma_{GB}\left(\frac{1}{r_1}+\frac{1}{r_2}\right) = \frac{\alpha\gamma_{GB}}{\overline{G}} = F_{GB} \qquad (2)$$

where ΔP is the pressure difference between adjacent grains, γ_{GB} is the grain boundary energy, α is a geometrical factor, $\overline{G}$ is the average grain size, r_1 and r_2 are the principal radii of curvature at a given point on the interface between the two grains and F_{GB} is the driving force.

GBs in ceramic materials are usually faceted and not completely curved, consisting of flat planes parallel to crystallographic planes of the material. As a result, the use of the concept of weighted mean curvature (WMC), according to which the GBs move in the direction of the weighted mean curvature in order to eliminate grain boundary area and reduce the system's excess energy [3], is commonly used.

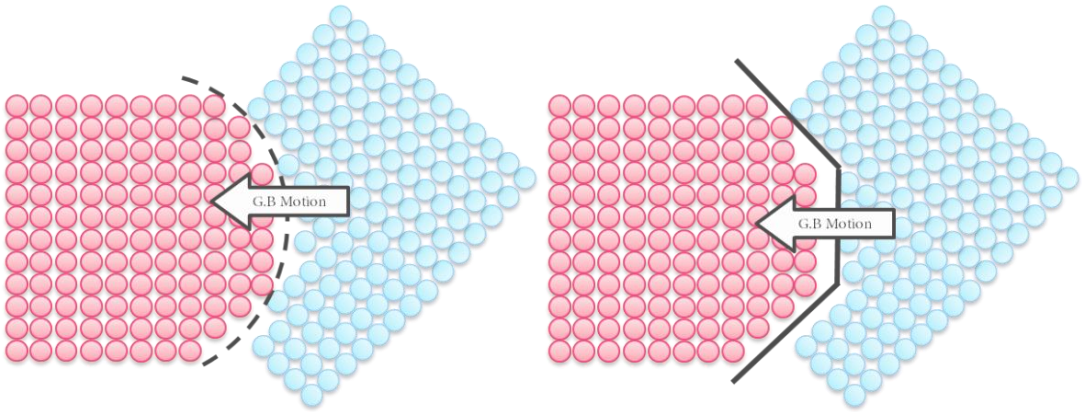

Figure 3: Schematic representation of (a) a curved and (b) a faceted GB motion during grain growth.

A recent work on Ni polycrystals by Bhattacharya et al. experimentally demonstrated that there is no correlation between grain boundary curvature and the direction/velocity of crystal growth [4]. Using high energy x-ray diffraction microscopy, they observed a correlation with the crystallographic properties of the grains and postulated that anisotropy of grain boundary energy and/or defect-mediated migration may play a role.

Another work by Muralikrishnan et al. found that flat boundaries in strontium titanate ($SrTiO_3$) move faster than curved boundaries. Additionally, 37% of the GBs they observed moved in the direction opposite to that of their curvature, which is contrary to the concept of weighted mean curvature [5].

1.2.2 Mechanism of Grain Boundary Motion

The atomistic mechanism by which atoms migrate across GBs was first suggested by Gleiter [6] using the terrace-ledge-kink (TLK) model, presented in Figure 4 [7], which was originally developed for crystal surfaces. This model cannot be applied directly to interfaces in polycrystalline materials because interfacial line defects are not pure steps/ledges. They're generally characterized by a step and/or dislocation component, and are called disconnections. Hirth and Pond later suggested that the mechanism for grain boundary motion involves the lateral movement of these linear defects in the plane of the grain boundary [8].

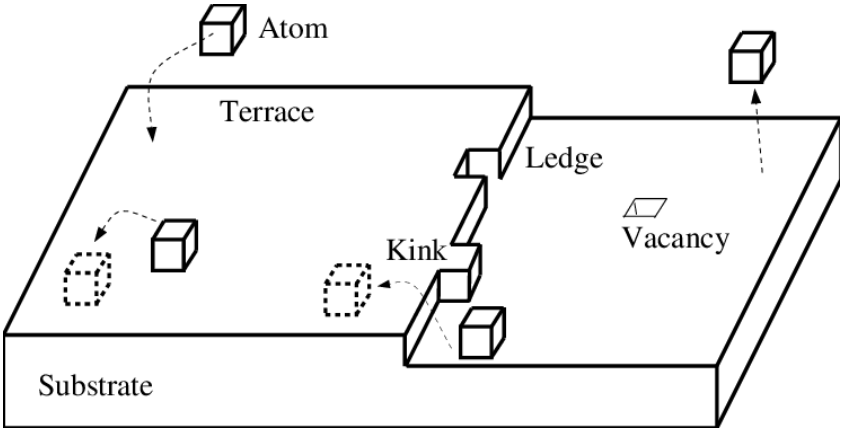

Figure 4: Schematic illustration of the TLK model for describing atom motion on surfaces, reproduced from [7].

This was experimentally demonstrated for $SrTiO_3$ by Sternlicht et al. , who used both ex-situ and in-situ high resolution transmission electron microscopy (TEM) [9]. Other experimental studies include those by Legros et al. [10] on nanocrystalline Al films, by Rajabzadeh et al. [11,12] on bicrystalline and polycrystalline thin Al films, and by Radetic et al. [13] on bicrystalline thin Au films. Combe et al. [14] used molecular simulation to show that GB migration occurs through the nucleation and motion of disconnections, and Han et al. [15] have recently extensively modeled the role of disconnections in grain growth.

1.2.3 Grain Boundary Mobility

Analysis of the grain boundary velocity can be challenging. The velocity of GBs (V_{GB}) can vary greatly between different systems. In order to compare between different systems, it is preferable to normalize V_{GB} by the driving force (F_{GB}) for grain boundary motion and define the grain boundary mobility M_{GB} [16]. In single-phase systems:

$$M_{GB} = \frac{V_{GB}}{F_{GB}} \tag{3}$$

Measuring the mobility of GBs allows for the comparison of different materials while considering variables like impurities, sintering conditions, initial powder grain sizes, etc. The velocity at which GBs move can be expressed as a change in the grain size as a function of time:

$$V_{GB} = \frac{d\overline{G}}{dt} \tag{4}$$

Combining equations (4), (3) and (2) while taking α=2 for equiaxed grains gives:

$$\frac{d\overline{G}}{dt} = \frac{2M_{GB}\gamma_{GB}}{\overline{G}} \tag{5}$$

By integrating equation (5), the following equation is obtained:

$$\overline{G}_t^{\,2} - \overline{G}_0^{\,2} = 4M_{GB}\gamma_{GB}t \tag{6}$$

where $\overline{G}_t^{\,2}$ and $\overline{G}_0^{\,2}$ are the average grain sizes at annealing times t and 0 (as sintered) and $M_{GB}\gamma_{GB}$ is the effective grain boundary mobility (sometimes called the reduced grain boundary mobility). $4M_{GB}\gamma_{GB}$ is also referred to as the grain growth constant (k_1).

This can be easily determined and comparable between different systems by simple grain size measurements as a function of time. The main drawback is that γ_{GB} cannot be separated from the mobility but, at the same time, measuring the grain boundary energy is challenging.

1.2.4 Solute Adsorption and Grain Growth

Truly pure, 100% undoped materials do notdo not exist. Powders always contain certain amounts of impurities, and more impurities can be introduced during any stage of the processing of ceramics. As such, it is important to keep the presence of impurities and dopants in mind in general, and when determining the effective grain boundary mobility in particular.

1.2.4.1 Solute Drag / Acceleration

Dopants or impurities present at a concentration below their solubility limit in polycrystalline materials can undergo equilibrium (Gibbsian) segregation to the GBs, driven by the reduction of the grain boundary excess energy. This creates a solute concentration profile near the GBs which can interact with the atoms in the vicinity or core of the grain boundary. A symmetrical solute concentration profile will be generated around a stationary grain boundary (ignoring non-symmetrical structural aspects of the

boundary). When a grain boundary begins to move during grain growth, the solute concentration profile can become asymmetrical, as presented in Figure 5:

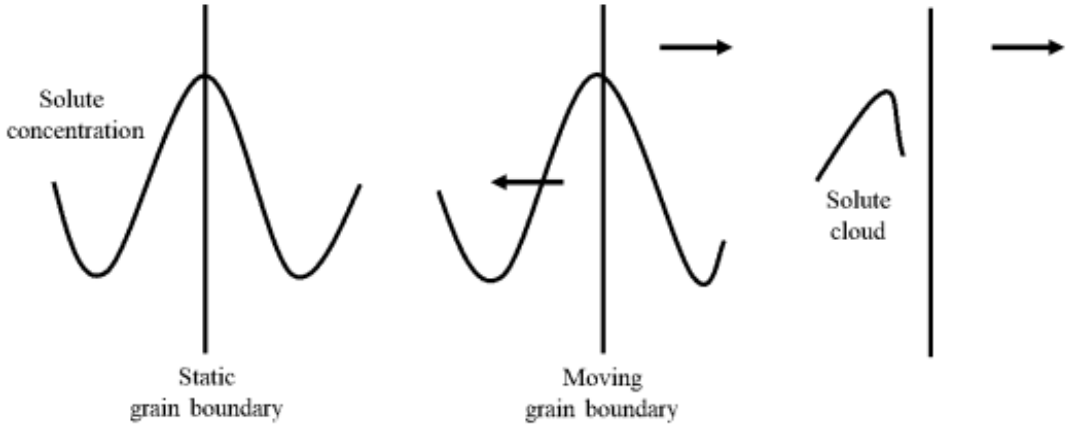

Figure 5: Schematic representation of the solute drag mechanism in polycrystalline ceramics; redrawn from [1].

The resulting asymmetry can generate a drag force (F_s) which reduces the grain boundary's velocity. If the driving force for grain growth is high enough, the grain boundary will break away from the solute cloud and return to its intrinsic mobility.

The drag force was calculated by Cahn [17]:

$$F_s = \frac{a_s C\infty}{1+(\beta V_{GB})^2} \tag{7}$$

where a_s is the solute drag force per unit velocity per unit solute concentration, C_∞ is the solute concentration in the bulk and β is the drift velocity at which the solute diffuses across the GB. The total drag force on a grain boundary in steady state is assumed to be the sum of the intrinsic drag force (F_0) and F_s, as described in Figure 6.

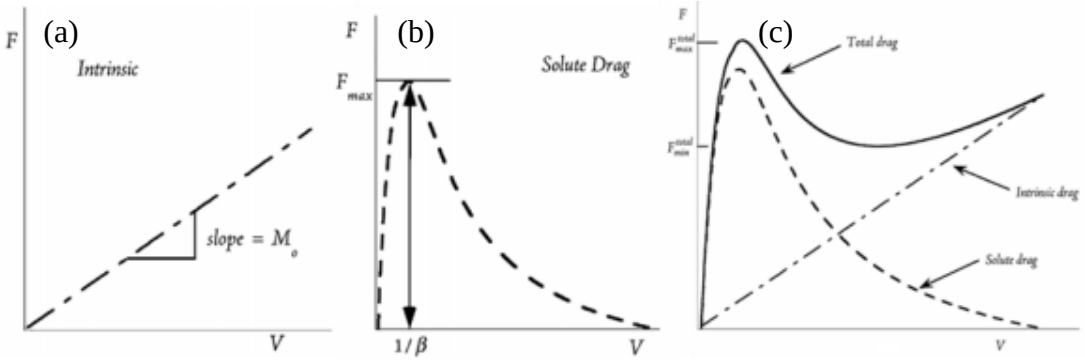

Figure 6: Driving force velocity behavior for (a) intrinsic migration, (b) solute drag only and (c) total force velocity; redrawn from [16].

This phenomenon is known as solute-drag. The presence of the solute near the grain boundary can result in a drag effect on the grain boundary, leading to a reduction in mobility. There have been studies, however, that have shown that the solute profile can also cause an increase in the grain boundary mobility [18,19,20,21,22,23].

1.2.4.2 Zener Drag

When the concentration of dopants or impurities is above their solubility limit, secondary phases form. The resulting precipitates can hinder grain boundary motion by pinning the GBs, as can be seen in Figure 7. This is known as Zener drag [1] and can also result from the interaction between GBs and pores [24].

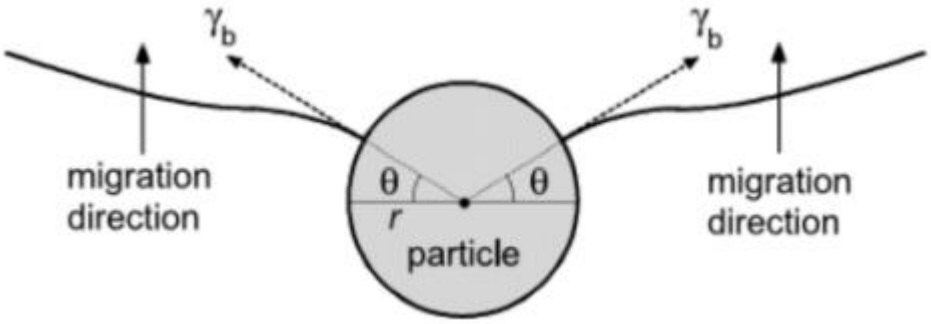

Figure 7: Schematic of the Zener drag effect where a particle of a secondary phase or a pore induces a retarding force on the grain boundary; reproduced from [1].

The drag force of a single precipitate/pore (F_z) can be expressed by [25]:

$$F_z = 2\pi r\gamma_{GB}\cos(\theta)\sin(\theta) = \pi r\gamma_{GB}\sin(2\theta) \quad (8)$$

where r is the precipitate/pore (particle) radius and θ is the angle shown in Figure 7.

The drag force is maximal when θ=45°:

$$F_z^{max} = \pi r\gamma_{GB} \quad (9)$$

Combining this with equation (3) , it is possible to express the grain boundary velocity under the Zener drag effect of N_z particles as:

$$V_{GB} = M_{GB}(F_{GB} - N_z \cdot F_z) \quad (10)$$

Similarly to grain boundary velocity, the velocity of a particle (V_p) is:

$$V_p = M_p \cdot F_p \quad (11)$$

where M_p is the mobility of the particle and F_p is the driving force for the motion of the particle.

There are three cases for an interaction between a grain boundary and a particle, as is detailed in Figure 8. When $V_{GB} > V_p$, the grain boundary will break away from the particle, which will become occluded. When it comes to pores, this is detrimental to the overall densification of the material.

If $V_{GB} = V_p$, the particle will remain attached to the grain boundary and move with it. The velocity of the grain boundary in this case will be:

$$V_{GB} = F_{GB}\left(\frac{M_{GB}M_p}{N_z M_{GB} + M_p}\right) \tag{12}$$

In this case, there are two possible scenarios:
When $N_z M_{GB} >> M_p$, the migration of the grain boundary is limited by the mobility of the particle (pore control).
$N_z M_{GB} << M_p$, the migration of the grain boundary is unaffected by the mobility of the particle (boundary control).

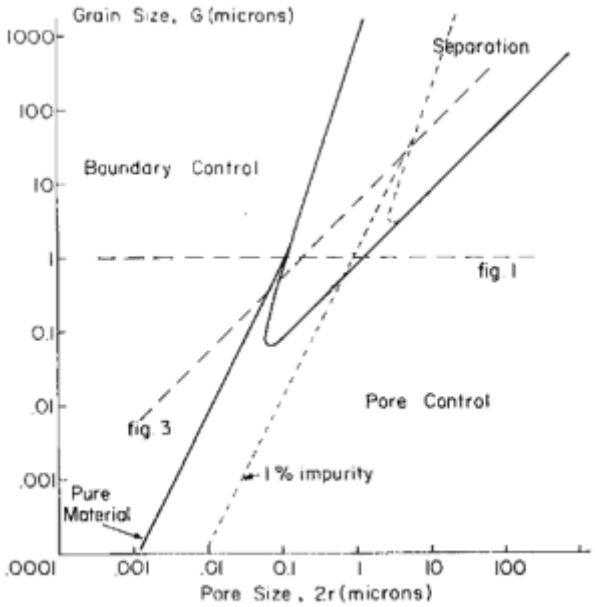

Figure 8: Pore boundary interaction as a function of grain and pore size, assuming pores migrate by surface diffusion; reproduced from [24].

1.3 Alumina

1.3.1 Crystallographic Structure

Alpha-alumina (α-Al_2O_3) is typically known as the stable structure of alumina, although various metastable structures exist [26]. It has a rhombohedral (corundum) unit cell with a trigonal symmetry (space group R $\bar{3}$C (No. 167)) and is commonly represented using a hexagonal unit for simplicity [27]. The hexagonal unit cell contains 12 aluminum atoms and 18 oxygen atoms [28] as can be seen in Figure 9.

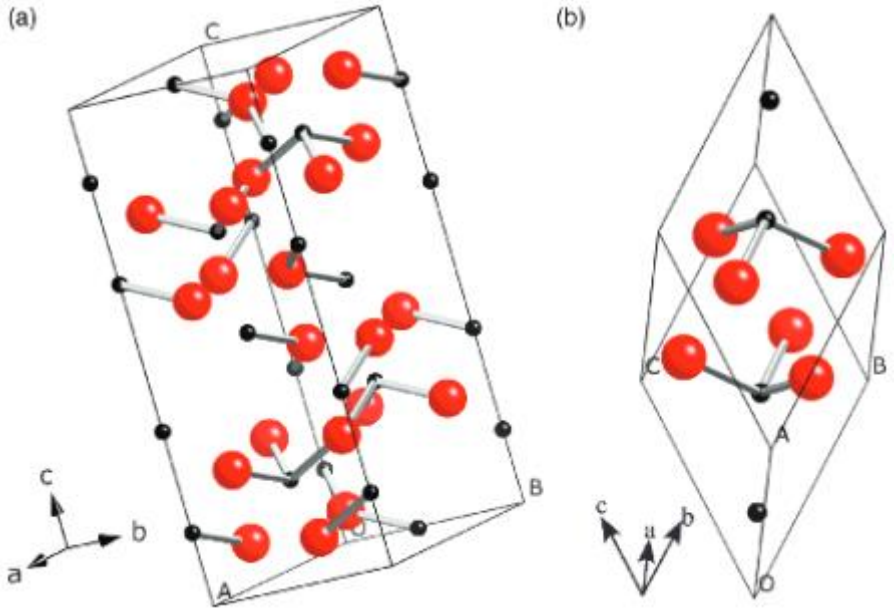

Figure 9: Schematic drawing of the hexagonal (a) and rhombohedral (b) unit cells of α-alumina. The black spheres represent aluminum cations and the red spheres represent oxygen anions; reproduced from [28].

When it comes to ceramic materials, α-alumina stands out because of its high wear resistance, heat conductivity, chemical inertness, hardness and electrical insulation. Its relatively low cost means it is widely used for a wide variety of applications. This makes it one of the most studied ceramics and a good model system for ceramic materials in general.

1.3.2 Dopants and Grain Boundary Mobility in Alumina

The significant influence of dopants on the sintering of alumina and its resulting properties was first shown by Coble [29], who demonstrated that doping alumina with MgO advanced the densification of the green body. The addition of Mg not only helped

in facilitating full densification but also in reducing the grain boundary mobility and suppressing grain growth. This allowed for the creation of high-density translucent alumina and has made doping alumina with Mg a standard practice during processing.

Roy and Coble later reported the solubility limit of MgO at 1630°C to be 300 ppm [30]. However, they did not actually measure the Mg concentration in their samples after sintering.

Bennison and Harmer doped alumina with 200 ppm of MgO and observed a decrease in the grain growth kinetics, as can be seen in Figure 10 [31]. They based their reported concentration on the amount added during the processing, and did not measure the content after sintering.

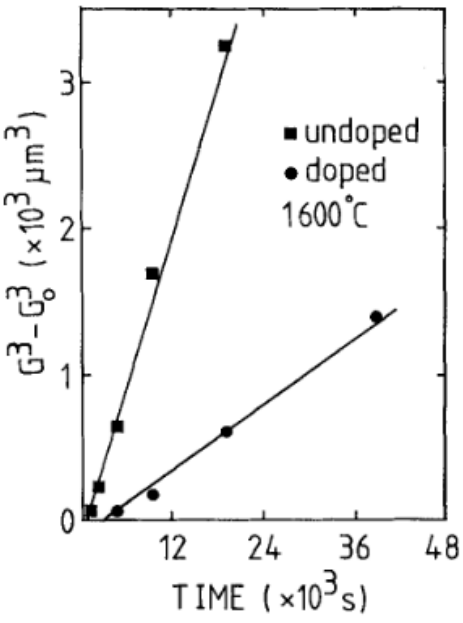

Figure 10: Grain growth kinetics of undoped and MgO-doped alumina; reproduced from [31].

Similarly, Rödel and Glaeser doped alumina with 250 ppm and also observed a decrease in the grain growth constant (k_1), but their concentrations were also reported based on the amount measured prior to sintering [32].

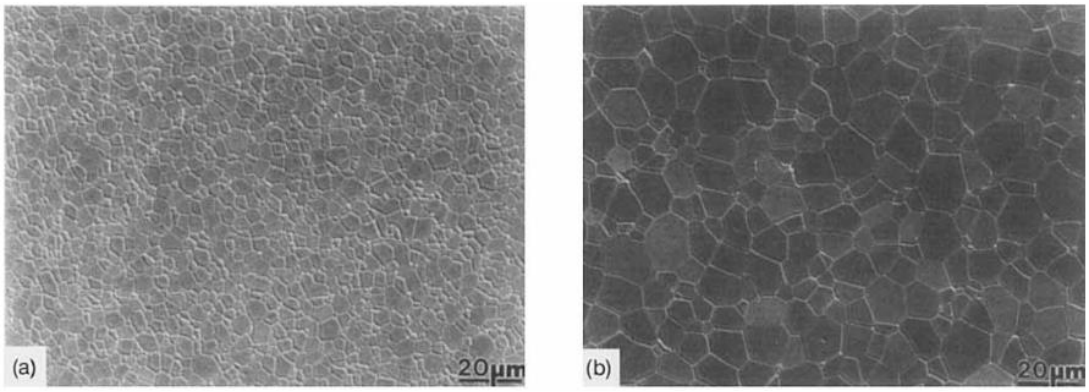

Figure 11: Grain structure of dense, MgO doped Al_2O_3 (a) as sintered and (b) after annealing for 7.5 hours at 1600°C in air; reproduced from [32].

Miller et al. measured the solubility limit of Mg at 1600°C using quantitative wavelength dispersive spectroscopy (WDS) and found it to be 132 ± 11 ppm [33]. Akiva et al. later examined the effects of Mg doping below the solubility limit and demonstrated a decrease in the mobility due to the solute drag effect [34].

Baik and Moon [35] demonstrated that the beneficial effect of MgO doping might be related to its effectiveness in controlling the segregation of Ca cations to the surfaces of pores and GBs. Ca is an example for a dopant (and usually labled an impurity) that causes the opposite effect than that of solute-drag.

Bae et al. [36] and Jung et al. [37] investigated the effect of CaO on abnormal grain growth in alumina. They measured the Ca concentration using inductively coupled plasma spectroscopy (ICP) and reported a critical Ca concentration of 30 ppm, above which abnormal grain growth occurs. Additionally, their results implied a linkage between the phenomenon and the formation of a stable intergranular glass phase with an estimated minimum thickness of 0.35 nm, assuming the composition of the glass was close to that of calcium hexa-aluminate ($CaO{\cdot}6Al_2O_3$). They acknowledged that the use of ICP to determine the chemical content means there were contributions to the reported Ca concentrations from both the GBs and the bulk of the alumina grains.

Assuming no Ca in solution in the grains and a hypothetical Ca concentration at the GBs, Altay and Gülgün found that, above a grain boundary concentration of Γ_{Ca}=3 atoms/nm^2, the morphology of the grains changed from equiaxed to elongated [38]. The actual Ca content was ***not*** measured.

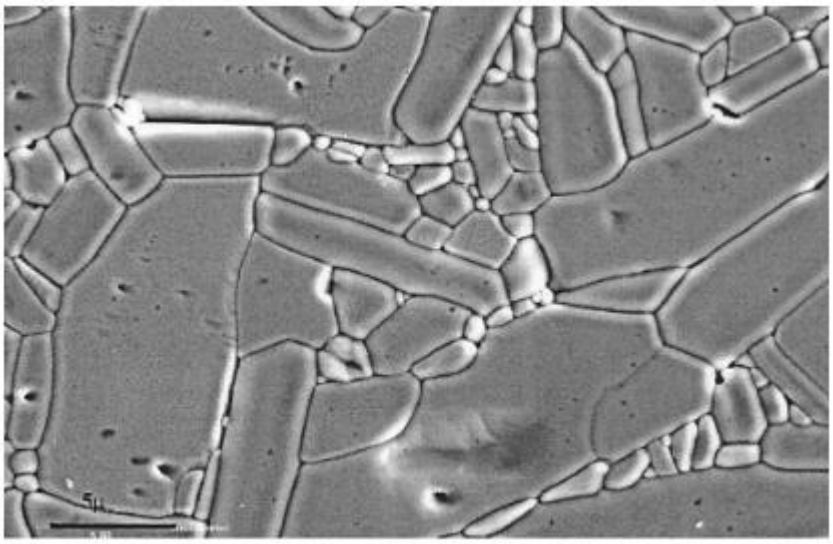

Figure 12: SEM micrograph of 344-ppm-Ca-doped α-Al_2O_3 sintered at 1500°C for 12 hours showing abnormally grown and elongated grains; reproduced from [38].

Akiva et al. measured the solubility limit of Ca at 1600°C using quantitative WDS and found it to be 51 ± 1 ppm [19]. Later, Ghosh et al. measured the solubility limits at 1400°C and 1500°C, also using quantitative WDS, and found them to be 32 ± 3 ppm and 45 ± 3 ppm, respectively [39].

It was reported by Bae et al. that increasing the SiO_2 concentration to above 300 ppm causes abnormal grain growth due to the formation of a liquid phase, indicating the presence of a secondary phase [40]. However, they did not measure the actual concentration. In Dillon and Harmer's work, an increase in the grain boundary mobility was observed after adding 200 ppm of SiO_2, but not by further increasing it to 500 ppm [41]. They considered 200 ppm to be the solubility limit. Both studies did not measure the actual Si concentrations.

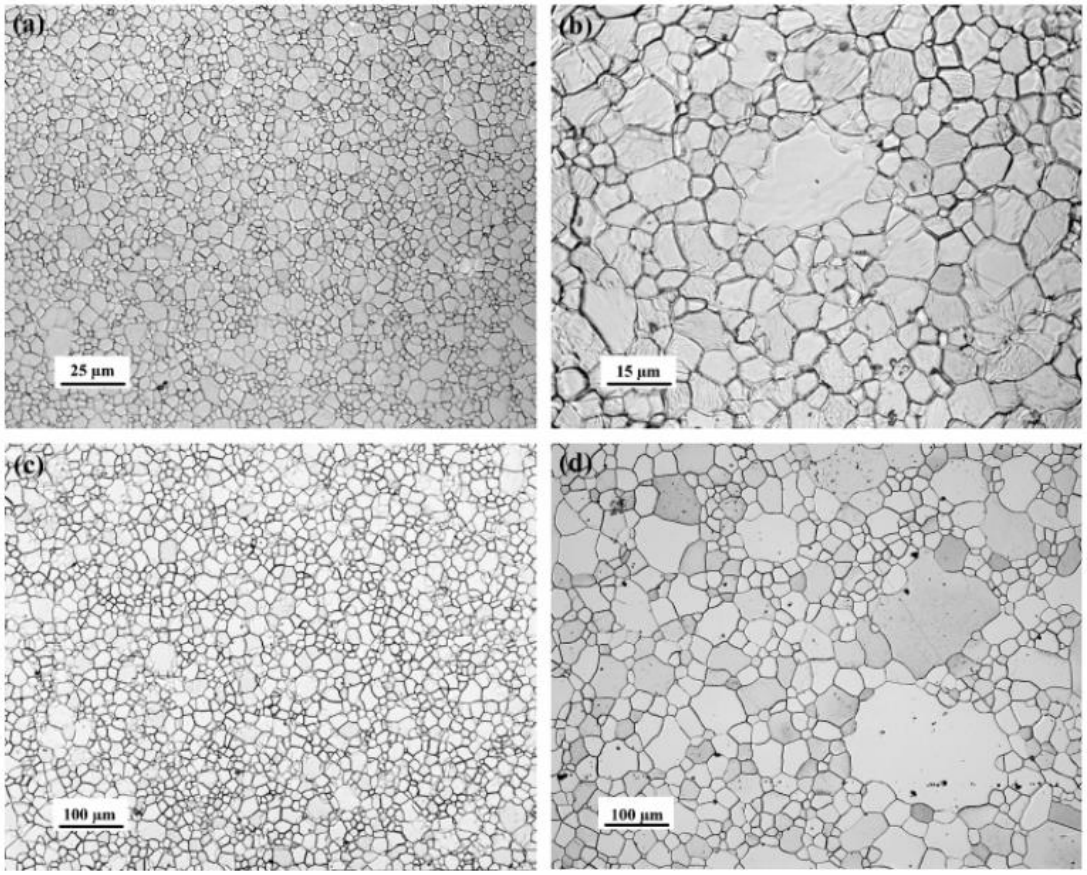

Figure 13: Representative optical micrographs of 200 ppm silica-doped alumina sintered at (a) 1300°C for 21 hours, (b) 1400°C for 50 hours, (c) 1500°C for 26 hours and (d) 1750°C for 6 minutes; reproduced from [41].

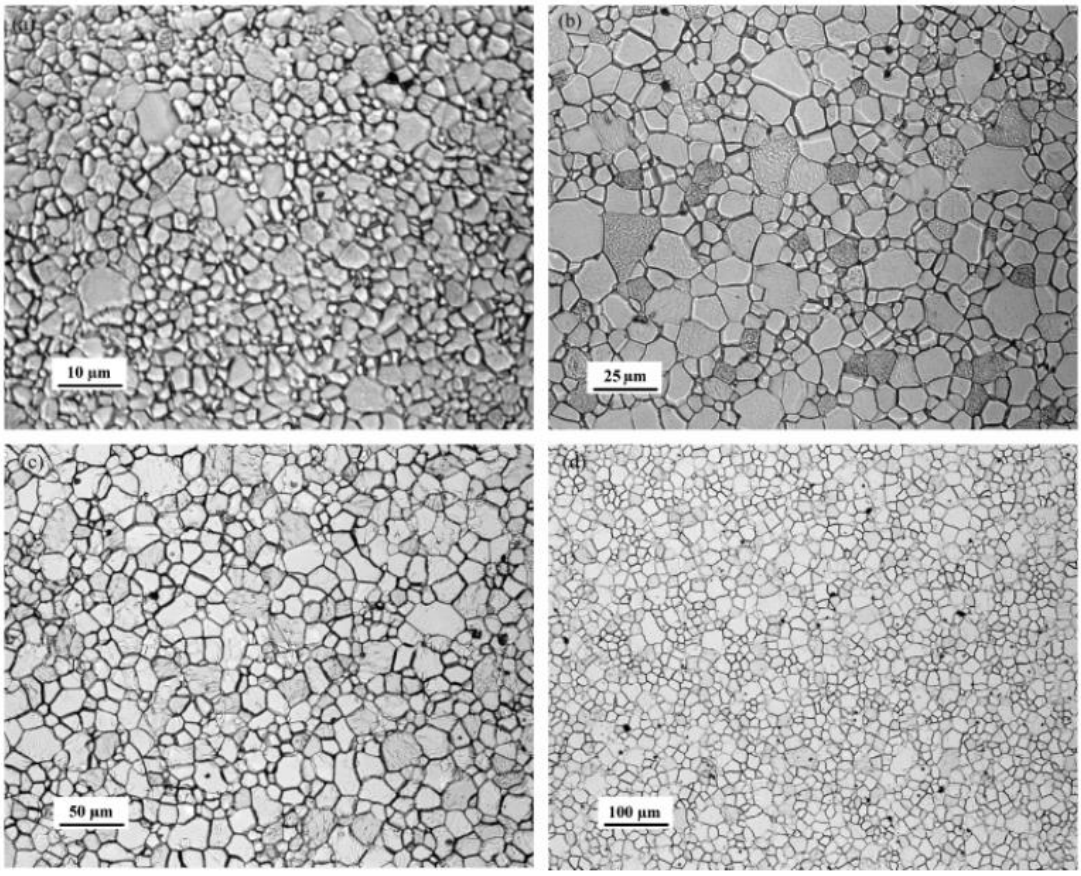

Figure 14: Representative optical micrographs of 500 ppm silica-doped alumina sintered at (a) 1300°C for 28 hours, (b) 1400°C for 50 hours, (c) 1500°C for 30 hours and (d) 1750°C for 9 minutes; reproduced from [41].

Moshe et al. measured the solubility limit of Si in alumina at 1600°C using quantitative WDS and found it to be 188 ± 7 ppm [42].

The solubility limits for Ca [19], Si [42] and Mg [33] at 1600°C are summarized in Table 1.

Table 1: Summary of the solubility limits of Ca, Si and Mg in alumina at 1600°C.

Element	Solubility Limit at 1600°C [ppm]
Ca	51 ± 2
Si	188 ± 7
Mg	132 ± 11

1.4 Field Assisted Sintering

1.4.1 Spark Plasma Sintering

In spark plasma sintering (SPS), the ceramic powder is placed inside a graphite die and between two graphite punches [43]. It is heated up quickly by passing an electric current through the die (and sometimes through the sample itself if it is conductive) while simultaneously being hot pressed. This rapid heating not only shortens the overall sintering time by increasing the heating rate but, in combination with the high mechanical pressure, causes densification to occur more rapidly and at a lower temperature. This has been demonstrated in both conductive and non-conductive materials [44].

Spark plasma sintering is carried out either in vacuum or an otherwise controlled atmosphere. A schematic drawing of an SPS system is presented in Figure 15.

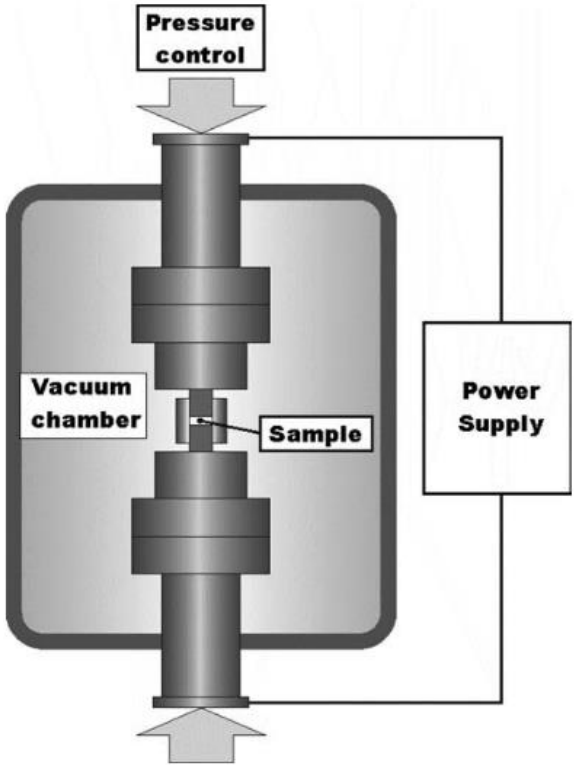

Figure 15: Schematic of the SPS apparatus; reproduced from [43]. Vacuum isn't always used. Sometimes controlled atmospheres like inert gases (e.g., argon) are employed.

While full densification can be achieved in a fraction of the time required for conventional sintering, SPS is expensive, as well as limited to small sample sizes and

conventional shapes, making it limited for mass-production. Additionally, densification can be inhomogeneous.

1.4.1.1 Spark Plasma Sintering of Alumina

Shen et al. conducted a systematic study of spark plasma sintering of alumina focusing on various parameters like the temperature, pressure, heating rates, holding time and DC pulse sequence [45]. Their data demonstrates an enhancement of both densification and grain growth by the SPS process, allowing them to fully densify alumina at a temperature as low as 1150°C and within minutes. With densification being more prominent in the initial part of the process, they were able to retain the original fine-grained structure by adjusting the temperature and holding time.

Kim et al. were able to sinter transparent alumina using spark plasma sintering at 1150°C (Figure 16) by adjusting the heating rates [46]. Chakravarty et al. investigated the effect of Mg doping on spark plasma sintering of alumina and were able to improve the densification, hinder grain growth and improve the overall mechanical properties [47].

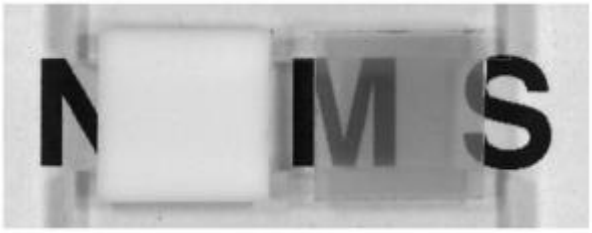

Figure 16: Alumina ceramics sintered by SPS at 1150°C at a heating rate of 100°C/min (left) and 8°C/min (right); reproduced from [46].

1.4.2 Flash Sintering

In flash sintering, a high DC voltage is applied to the green body during heating. Upon reaching a combination of a critical voltage and temperature (the critical point), dielectric breakdown occurs, resulting in what is believed to be joule heating, and densification occurs within seconds [48]. The setup for flash sintering can vary, as is visualized in Figure 17.

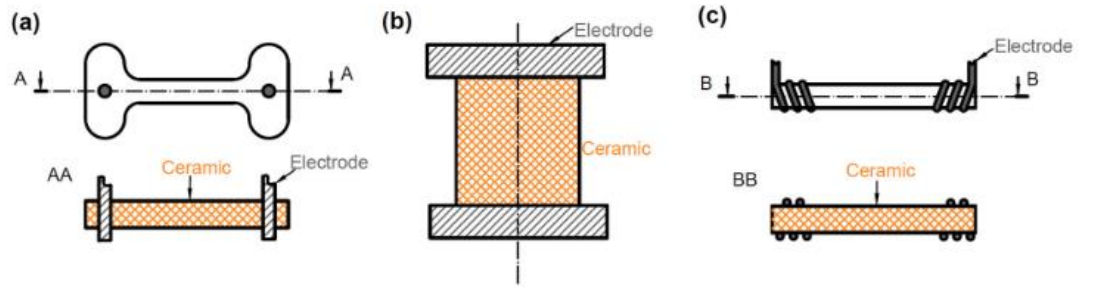

Figure 17: Typical sample geometries and experimental setups for flash sintering experiments: (a) dog bone, (b) pellet and (c) rod; reproduced from [48].

Much like with SPS, full densification is also achieved in a fraction of the time required for conventional sintering, but the applicability for mass-production is limited. The Joule heating tends to lead to inhomogeneous densifications and microstructures, making it difficult to control and engineer the material's properties.

1.4.2.1 Flash Sintering of Alumina

Cologna et al. attempted to flash sinter undoped alumina and saw no difference when employing electric fields as strong as 1000 V/cm [49]. When adding 0.25 wt.% MgO, they were able to obtain dielectric breakdown (see Figure 18). Biesuz and Sglavo later attempted to flash sinter undoped alumina and succeeded (see Figure 19), however their starting powders contained more impurities [50]. Additionally, differences between the two groups' green bodies may explain the difference in their overall results.

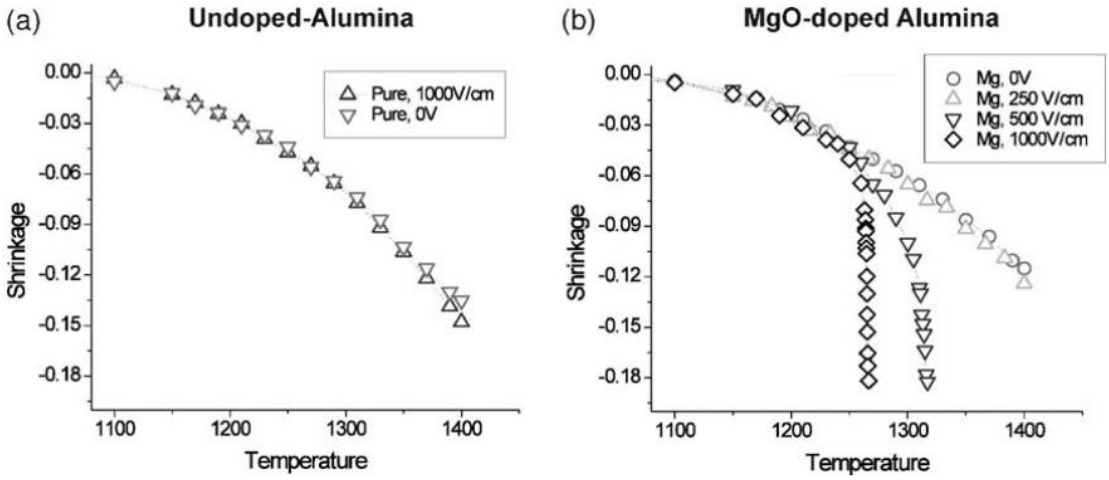

Figure 18: Shrinkage curve for (a) "pure" (undoped) and (b) Mg-doped alumina under varying electric field strengths; reproduced from [49].

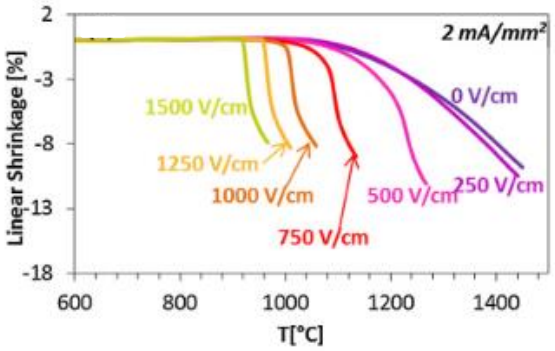

Figure 19: Shrinkage curve for undoped alumina under varying electric field strengths; reproduced from [50].

1.4.3 Field Assisted Grain Growth

There have been claims that field assisted sintering inhibits grain growth. To address this, Marder et al. carried out annealing experiments on alumina using an SPS apparatus to evaluate the influence of an electric field on grain growth [51]. In comparison to annealing done without an electric field, the effective grain boundary mobility *increased* by two orders of magnitude, from 10^{-16} m^2/sec to 10^{-14} m^2/sec, indicating that the electric field may lower the activation energy for disconnection formation and/or motion. In addition, after a prolonged annealing under the electric field (see Figure 20), a variation in the average grain size was observed between the grains adjacent to the different electrodes. They attributed this to the potential diffusion of positively charged oxygen vacancies towards the negative electrode, resulting in accelerated grain growth.

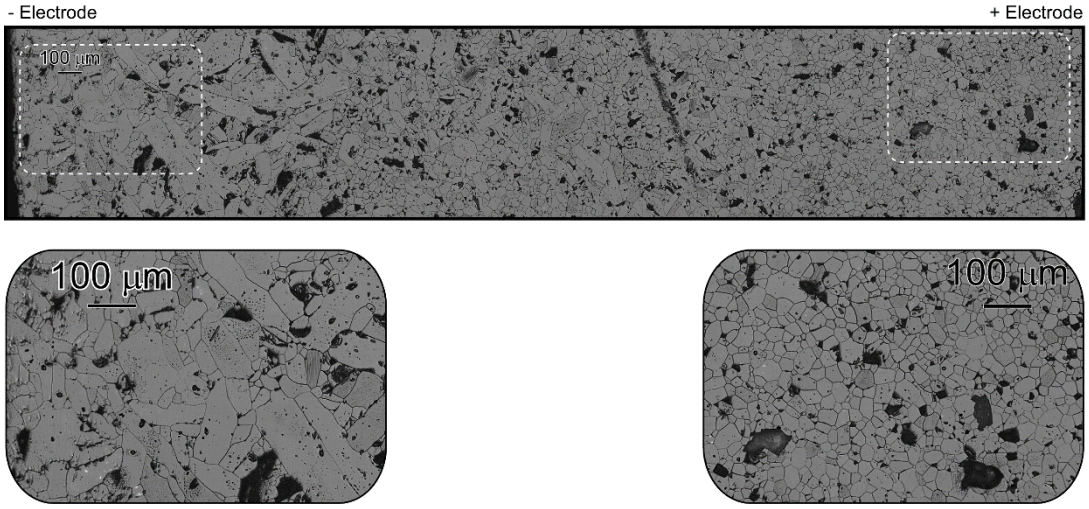

Figure 20: Assembled optical micrographs showing the full cross-section of an undoped alumina sample annealed by SPS for 8 hours at 1600°C. The area to the left was towards the bottom (negative) electrode in the SPS apparatus, and the area to the right towards the top (positive) electrode. The two inserts represent two enlarged areas in the specimen (marked by the dotted rectangles); reproduced from [51].

Jeong et al. wished to study the influence of a static field on the migration of GBs in alumina [52]. To do this, they fabricated undoped alumina samples where one half of the sample consisted of considerably larger grains, meaning the grain boundary at the interface between those two regions would move into the small-grained region. They positioned their samples between two Pt electrodes in a way that resembles a flash sintering setup, as is presented in Figure 21.

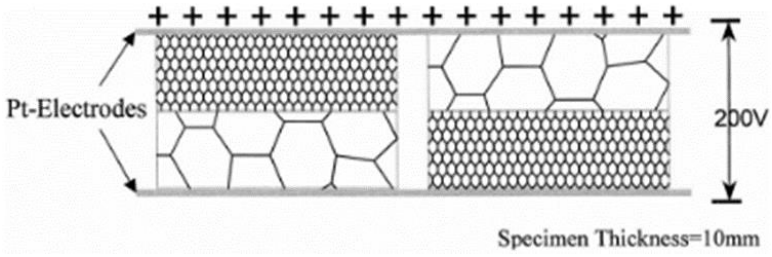

Figure 21: Schematic illustration of the experimental setup used by Jeong et al.; reproduced from [52].

They measured the grain boundary's migration distance (ΔL) into the small-grained region of the samples without an electric field and when applying the electric field in two different directions. Their results are presented in Figure 22. They observed an increase in the grain boundary mobility when applying the positive bias to the small-grained region and a decrease when applying it to the large-grained region. Like the

work conducted by Marder et al., this also indicates that the presence of an electric field can lead to an inhomogeneous microstructure.

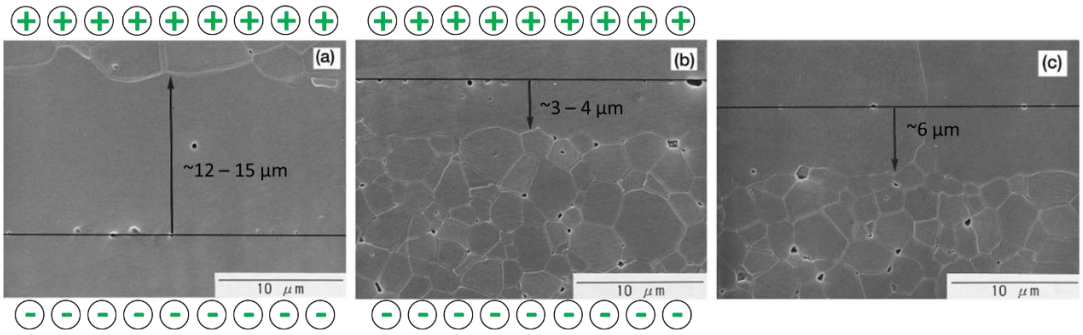

Figure 22: Micrographs showing the grain-boundary migration during the heat treatment at 1600°C for 2 hours under an applied bias of 200V ((a) positive bias applied to the small-grained region, (b) negative bias applied to the small-grained region and (c) without any bias voltage); reproduced from [52].

The influence of an electric field of grain growth was explored in other materials. It was observed for $SrTiO_3$ by Rheinheimer et al. who, while demonstrating a clear influence, did not measure the mobility directly from their results [53,54]. As such, actual values cannot be compared. Hughes et al. observed that the local oxygen vacancy concentrations are affected by the application of the electric field, which influences the ordering of the oxygen sublattice and the structure of the GBs while the misorientation angles remain unchanged [55,56].

In a study on $MgAl_2O_4$ spinel, Qin et al. showed that strong fields (>1000 V/cm) have an effect on both densification and grain growth during sintering [57]. However, they did not detect a change in the average grain size when annealing fully dense samples at varying field strengths compared to without a field. Their publication makes it unclear whether they compared the average grain size between different areas of their samples in different proximities adjacent to their electrodes (like Marder et al.), making it impossible to come to a decisive conclusion.

2. Research Goals

The main goal of this research is to understand the influence of a static electric field on grain growth in dense alumina, for undoped alumina and alumina doped with Ca below the solubility limit. By measuring the effective grain boundary mobility in undoped and Ca-doped alumina with and without an applied external DC electric field, this work aims to validate the influence of the field on grain growth.

The application of the field is done in attempt to separate the Ca cations from their charge compensating oxygen vacancies, correlating the effect of the field on grain growth to the local dopant/impurity concentrations.

3. Experimental Methods

3.1 Processing of Alumina

To produce polycrystalline undoped and Ca-doped alumina samples, 150 g of high purity (99.995%) α-Al_2O_3 powder with an average particle size of 300 nm (CERALOX AHPA 0.5, Tucson, AZ [58]) was dispersed in 70 g of distilled water. For Ca-doped alumina, 0.150 g of calcium nitrate tetrahydrate ($Ca(NO_3)_2 \cdot 4H_2O$, Carlo Erba Reagents, Milan, Italy [59]) was added to the dispersion.

The alumina slurries were mixed for 72 h using a ball-milling system at a rate of 350 rpm. Miller et al. observed that using ZrO_2 milling balls could contaminate the alumina with up to 50 ppm of zirconium, so the mixing process was conducted without milling balls [33]. Instead of chemical deflocculants, so as to avoid contamination, analytically pure HCl was added to adjust the pH to approximately 4 to deflocculate the suspensions and avoid agglomeration of the alumina particles.

After mixing, green bodies were formed using vacuum filtration in air at room temperature, followed by drying in ambient for 1 week. Once dry, the green bodies were further dried in air at 40°C for 5 hours. Sintering was then done in air at 1600°C for 2 hours with a heating/cooling rate of 10 °C/min.

Prior to the annealing treatments, smaller samples were cut out of the bulk of the sintered slips and the density was measured. After the annealing treatments, the cross sections of the samples were mechanically polished using a diamond suspension on polishing cloths. The starting diamond size was 125 μm and the final diamond size was 0.25 μm. Another piece of each sintered master slip was polished to perform wavelength dispersive spectroscopy (WDS) measurements to confirm the Ca-doped alumina is below the 1600°C solubility limit of Ca in alumina.

To perform grain size measurements using scanning electron microscopy (SEM), the polished samples were thermally etched at 1250°C for 2 hours to induce grain boundary

grooving. The polished WDS samples were not thermally etched so as to avoid any potential change in the chemical content of the sintered material.

3.2 Annealing Setup

For the experimental configuration, the goal was to put together a system similar to that used for flash sintering and to avoid inducing dielectric breakdown based on what was previously observed by Cologna et al. [49] and Biesuz and Sglavo [50] when flash sintering alumina. To do this, two electrodes were fashioned by cutting sintered, undoped alumina into disks.

Conductive platinum paste ink (COL-INT TECH, Irmo, SC [60]) was used to coat one side of each disk. The platinum paste layers were then heat treated (see the annealing treatment in Figure 23 and a SEM micrograph of the annealed Pt paste in Figure 24) to braze the platinum to the alumina disk:

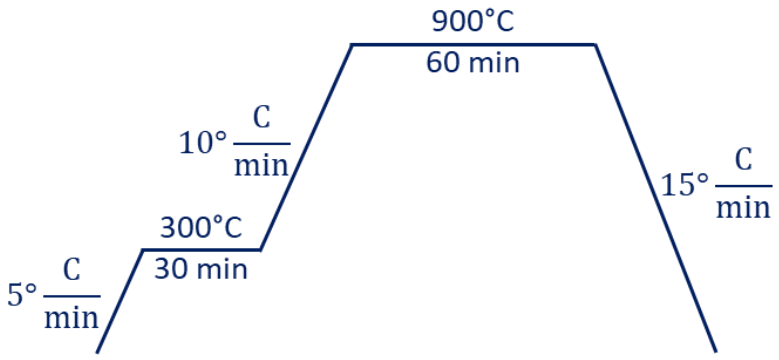

Figure 23: The heat treatment profile for the brazing of the platinum paste.

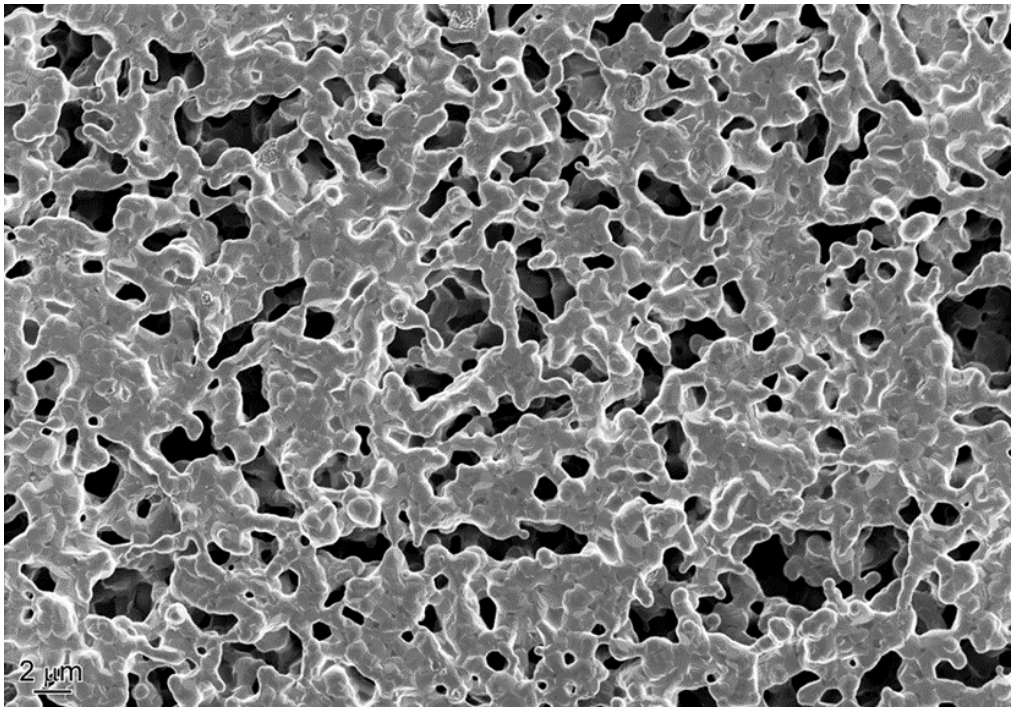

Figure 24: Secondary electron (SE) SEM micrograph of the platinum paste after the heat treatment.

After brazing the first layer, pure (99.95%) platinum wire, 0.813 mm in diameter (Surepure Chemetals, L. L. C., Florham Park, NJ [61]) was passed through thin alumina tubes and placed on top of the initial platinum layer, as can be seen in Figure 25. An additional layer of Pt paste was then applied and a heat treatment following the process described in Figure 23 was repeated to braze the Pt wire to the alumina disk.

Figure 25: Photograph of Pt wire brazed to an alumina disk.

In practice, because alumina is non-conductive at 1600°C, it is the platinum paste layers that act as electrodes during the annealing treatments.

To perform the annealing treatments at 1600°C, the electrodes and samples were placed inside a sapphire die (GAVISH Sapphire Products, Bedform, NH [62]), with the Pt covered sides facing outwards and away from the sample, as shown in Figure 26 and detailed in Figure 27. This was done to ensure the samples were stationary within the field and that the value of the field remained constant throughout the thermal treatments. The sapphire die was then positioned in the middle of a tube furnace.

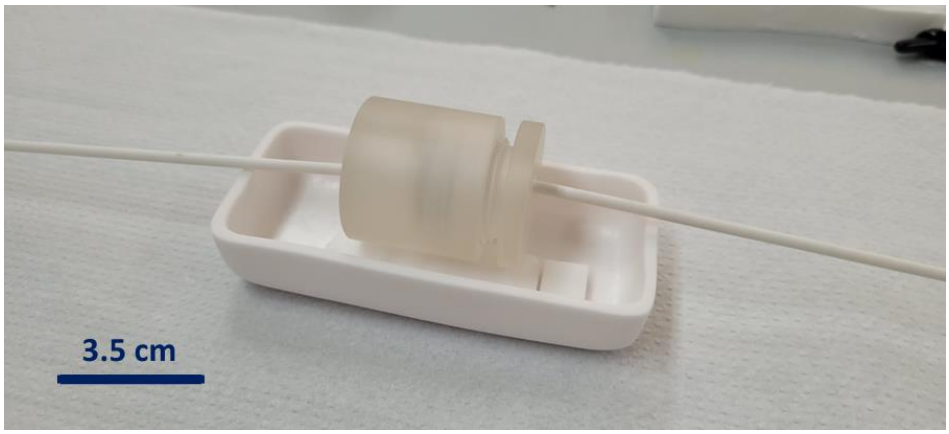

Figure 26: Photograph of an alumina sample positioned between the two electrodes inside the sapphire die.

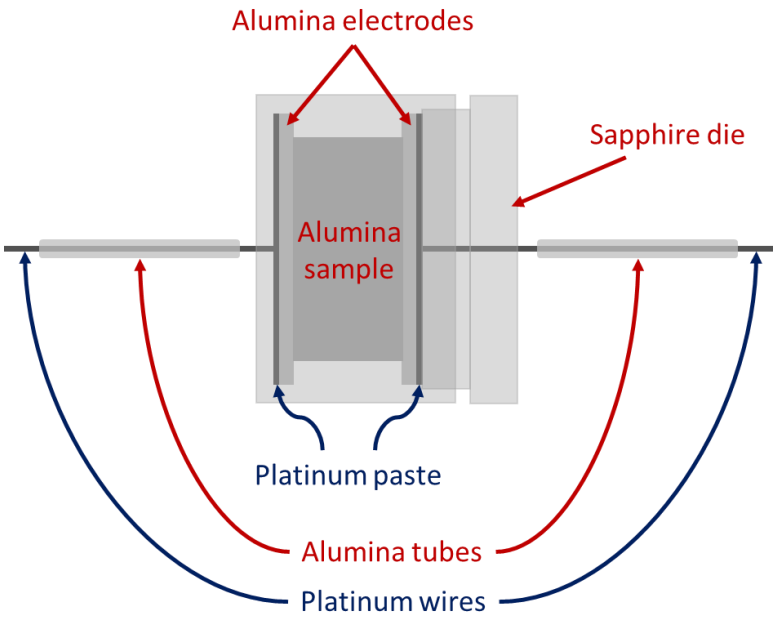

Figure 27: Schematic illustration of the experimental setup. The sample is pressed between the two alumina electrodes, with the Pt paste brazed sides of the electrodes facing outwards.

Therefore, the value of the field is the applied voltage divided by the total width of our alumina electrodes and the sample between them.

Prior to the annealing experiments, the tube furnace temperature was calibrated using a thermocouple. It was found that the furnace temperature had to be set at 1612°C so as to reach a temperature of 1600°C at the center of the tube, where the samples were located.

The annealing treatments were carried out in air following the scheme depicted in Figure 28, with the external static electric field being turned on/off at the beginning/end of the dwell time at 1600°C, respectively. The power source was monitored throughout the process and no current fluctuations indicating dielectric breakdown of air was observed.

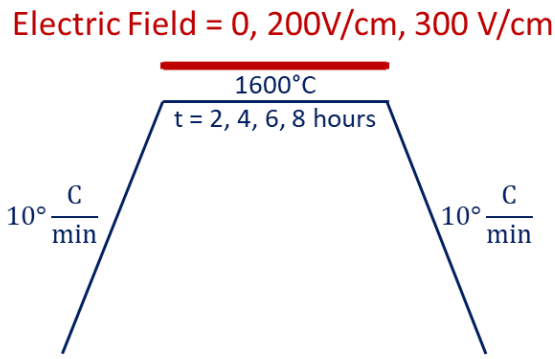

Figure 28: The heat treatment profile for the annealing treatments.

One undoped and one Ca-doped sample was heated to 1600°C and immediately brought back down to room temperature (no dwell time) to account for the influence of the heating/cooling process on the average grain size. The average grain size of these samples was taken as t=0 when extracting the effective grain boundary mobilities.

3.3 Characterization

3.3.1 Density Measurements

The density of the alumina slips (ρ) was calculated using the Archimedes' method following ASTM standard c 20-92 for a few pieces and calculating an average:

$$\rho = \frac{\left(\frac{D}{W-S}\right)}{\rho_{Al_2O_3}} \qquad (13)$$

where D is the dry weight of the piece, W is the saturated weight of the piece, S is the suspended weight of the piece and $\rho_{Al_2O_3}$ is the theoretical density of alumina (3.97 g/cm^3).

3.3.2 Scanning Electron Microscopy

SEM was used to measure the average grain size as a function of annealing time. The measurements were acquired using the Zeiss Ultra-Plus field emission gun SEM (Oberkochen, Germany) by acquiring secondary electron (SE) micrographs of polished cross-sections. The micrographs were obtained using an Everhart Thornley detector at working distances between 3-5 mm and accelerating voltages between 1.5 – 2 KeV.

Samples were prepared for SEM by cutting out a bulk piece from the samples, as is depicted in Figure 29.

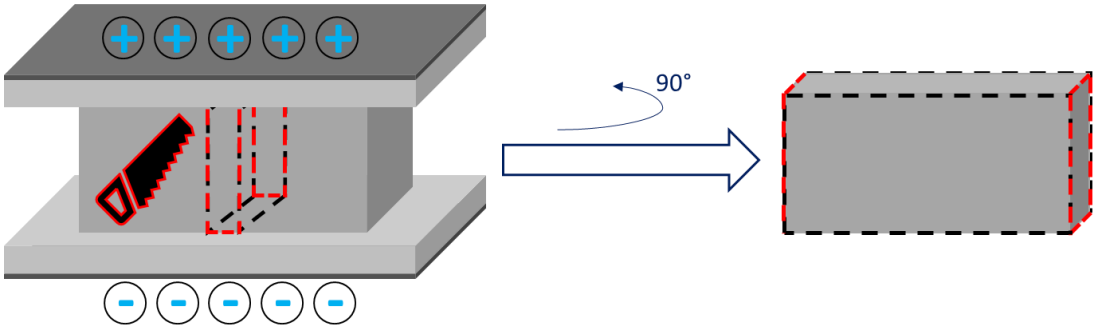

Figure 29: Schematic illustration of acquiring of a polished cross-section from an annealed alumina sample. A piece of each sample was cut out and polished in a way that the cross section was from the inner region of the samples and spanned the entire distance from one electrode to the other.

It was found during the mechanical polishing process that the semi-automated system available in our academic department introduced dynamic loading on the samples, resulting in grain boundary cracking and extraction of alumina grains (the so called “pull-out” effect). This wear debris also scratched the surface of the polished samples. This will be demonstrated by SEM in the Results chapter of this work. To confirm the samples are indeed dense (corroboration for the results of the density measurements), a dual-beam Xe FIB (Thermo Fisher Helios 5 Plasma Focused Ion Beam (PFIB)) was used to ion-polish a sample to a depth of the order of the grain size.

3.3.2.1 Grain Size Analysis

For effective grain boundary mobility measurements, micrographs were obtained from certain locations in the samples annealed under a field in regard to the distance adjacent to the electrodes. The linear intercept method [63] was used to determine the grain size, and a correction factor of 1.56 was applied given the 2D analysis on a 3D microstructure [64].

At least 700 grains were measured to calculate the effective grain boundary mobility for each annealing time and "area" of a sample, when relevant, using equation (6). For samples annealed under a field, measurements were done at distances of 100 μm adjacent to the positive and negative electrode and at the center of the sample, making for 3 sets of measurements per sample. For samples annealed without a field, only one set of measurements was obtained (from cross-sections from the center of the samples).

3.3.3 Wavelength Dispersive Spectroscopy

The concentration of dopants and impurities were measured using WDS (Oxford Instruments, High Wycombe, U.K.) mounted on a scanning electron microscope (ThermoFisher Prisma E-SEM).

The WDS measurements were conducted at a working distance of 10 mm, a magnification of x20,000 and using a spot size of at least 8.5, which is unitless and apparatus-dependent, aiming for a probe current of 50 nA or higher. The measurement time of a single measurement was 20 seconds and the accelerating voltage was 25 kV. 30 measurements were taken for each dopant in a given sample or "area" of a sample.

Diopside ($MgCaSi_2O_6$) was used as a standard when measuring Ca, Si and Mg. A pure platinum standard was used to determine whether platinum from the platinum paste on the electrodes had diffused into the samples. For Ca and Si measurements, a polyethylene terephthalate (PET) crystal was used as a monochromator. For Mg measurements, a thallium acid phthalate (TAP) crystal was used. For Pt, a lithium fluoride (LiF) crystal was used.

The concentration of a given dopant/impurity was determined using:

$$C = k \cdot C_{std} \cdot g_{ZAF} \tag{14}$$

where C_{std} is the concentration of the element within the standard, $k=I_{sample}/I_{std}$ is the ratio between the measured peak intensity of the sample (I_{sample}) and that of the standard (I_{std}) and g_{ZAF} is the ZAF correction factor calculated using the XPHI software [65].

The detection limit is important when attempting to detect and quantify the presence of dopants and impurities, especially when it comes to very small concentrations. Measuring the experimental detection limit for a given element and set of measurements is crucial. When looking at a measured concentration of 4 ppm, for example, reporting this value would be incorrect if the detection limit is 6 ppm. At the same time, we can never rule out the presence of a dopant/impurity below the limit we can detect. In this hypothetical example, there can be up to 6 ppm in our sample.

Assuming a Poisson distribution for the background intensity, with a confidence probability of 97.5%, the detection limit is:

$$C_{limit,0.975} = C_{std} \cdot g_{ZAF} \cdot \frac{2\sqrt{2I_{bgd}}}{\sqrt{m\tau}I_{std}} \tag{15}$$

where m is the number of measurements, I_{bgd} is the intensity of the background, and τ is the time of a single measurement.

The detection limit was determined for every set of measurements for a given session on the microscope, for every element in question.

4. Results

4.1 Undoped and Ca-Doped Alumina: As-Sintered

4.1.1 Density and Microstructure

The relative density of the undoped alumina was measured to be 98.2 ± 0.2% and the relative density of the Ca-doped alumina was measured to be 98.6 ± 0.4%. The microstructures of undoped and Ca-doped alumina samples after sintering (before annealing treatments to promote grain growth) are presented in Figure 30 and Figure 31, respectively.

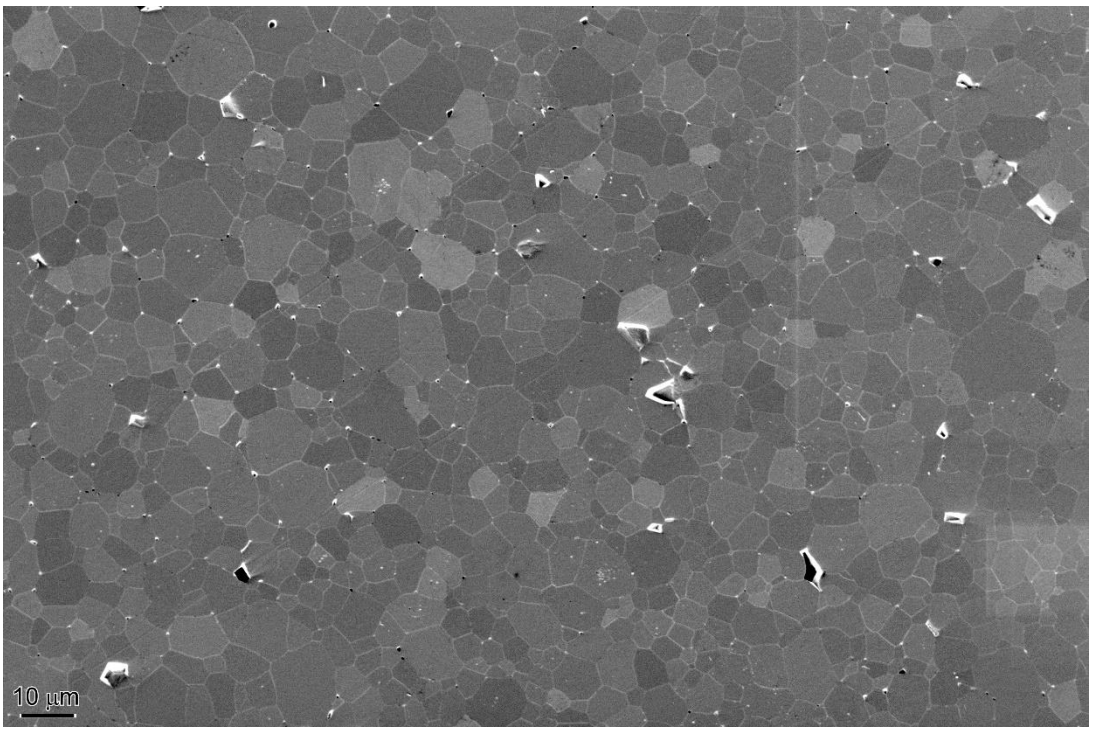

Figure 30: SE SEM micrograph (polished and thermally etched cross-section) of the microstructure of undoped alumina sintered in air at 1600°C for 2 h, and then heated up to 1600°C again and immediately cooled back down to room temperature after sintering.

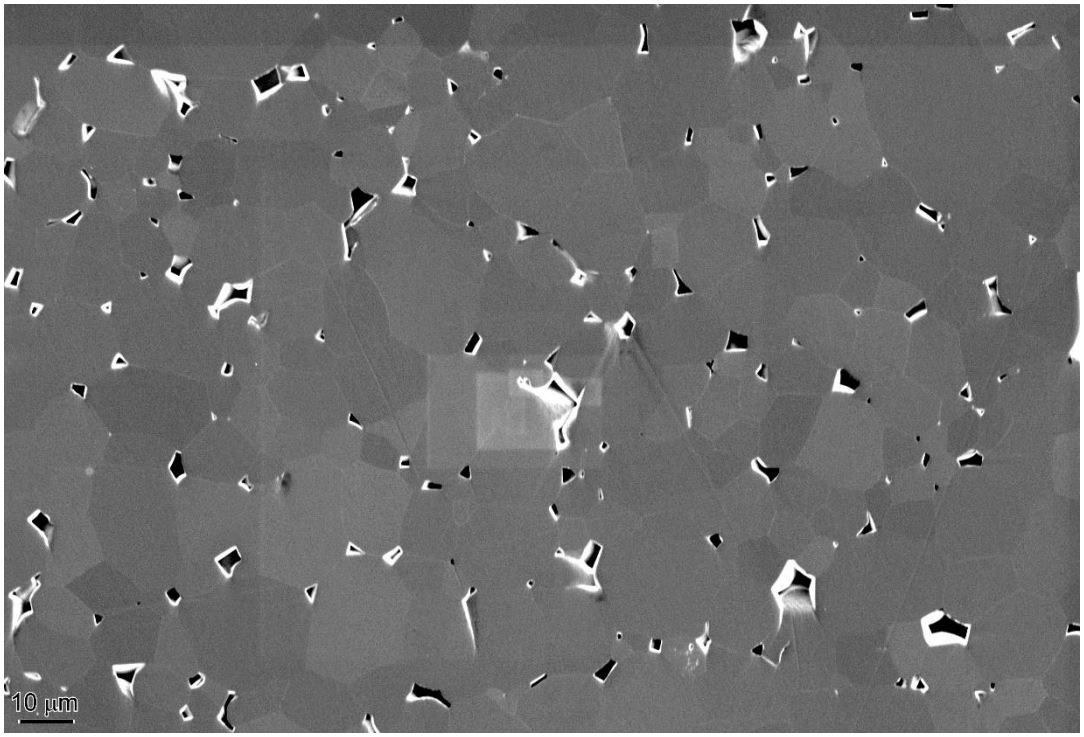

Figure 31: SE SEM micrograph (polished and thermally etched cross-section) of the microstructure of Ca-doped alumina, as sintered.

From the micrographs, it can be seen that the samples are dense (except for the pull-out damage), and that the grains have an equiaxed morphology. Some pores can be seen, while the "faceted pores" are grain pull-outs that result from impact fracture during the polishing process. Additionally, the polishing process left residual scratches, as is particularly prominent in Figure 30.

Mechanical alignment of the polishing system failed to reduce the number of pull-outs, and to corroborate the density measurements with the SEM micrographs, the sample presented in Figure 31 was *ion-polished* to a depth of the order of the grain size using a Xe FIB. An example is presented Figure 32, which was acquired using incident electrons immediately after FIB polishing.

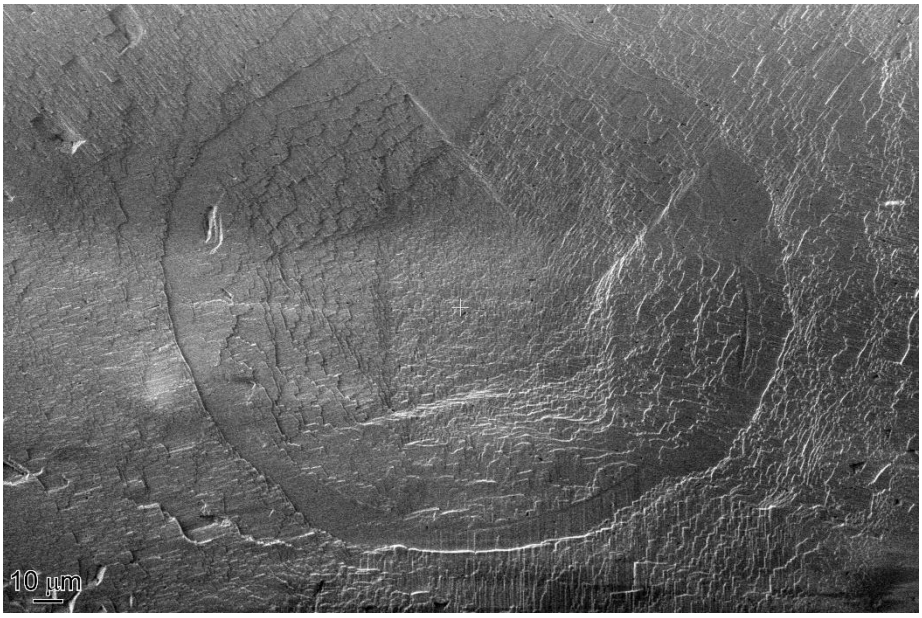

Figure 32: Low magnification SE SEM micrograph acquired from the dual-beam Xe FIB using incident electrons, from a Ca-doped sample after ion polishing to remove pull-out damage. Ion polishing was done at a 6° angle and a current of 60 nA, in the circular region towards the center of the micrograph.

A higher magnification micrograph (Figure 33) acquired during the FIB polishing process shows the typical "curtaining" effect from ion milling. Final low angle polishing was used to remove most of the curtaining effect, and resulting in an etching rate of the GBs which is different than the grains, making it possible to discern the grain size, residual pores, and residual pull-out damage (see Figure 34). While the FIB polishing demonstrates that our samples are dense (the large pores seen by SEM are mechanical pull-out that occurred *after* the annealing treatments), it is too time consuming to serve as an alternative to mechanical polishing.

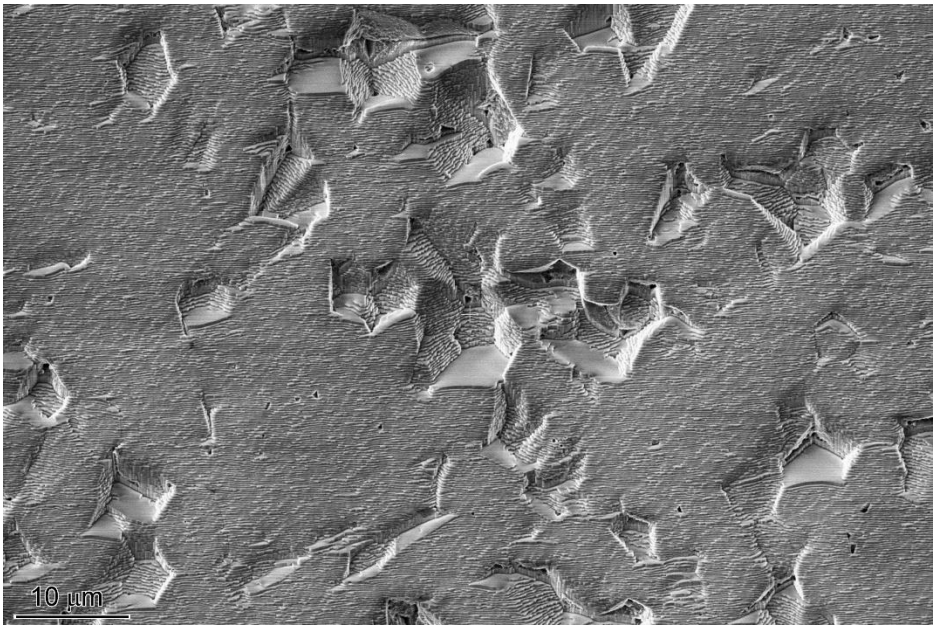

Figure 33: SE SEM micrograph acquired from the dual-beam Xe FIB using incident electrons, from a Ca-doped sample after ion polishing to remove pull-out damage. Ion polishing was done at a 38° angle and a current of 60 nA.

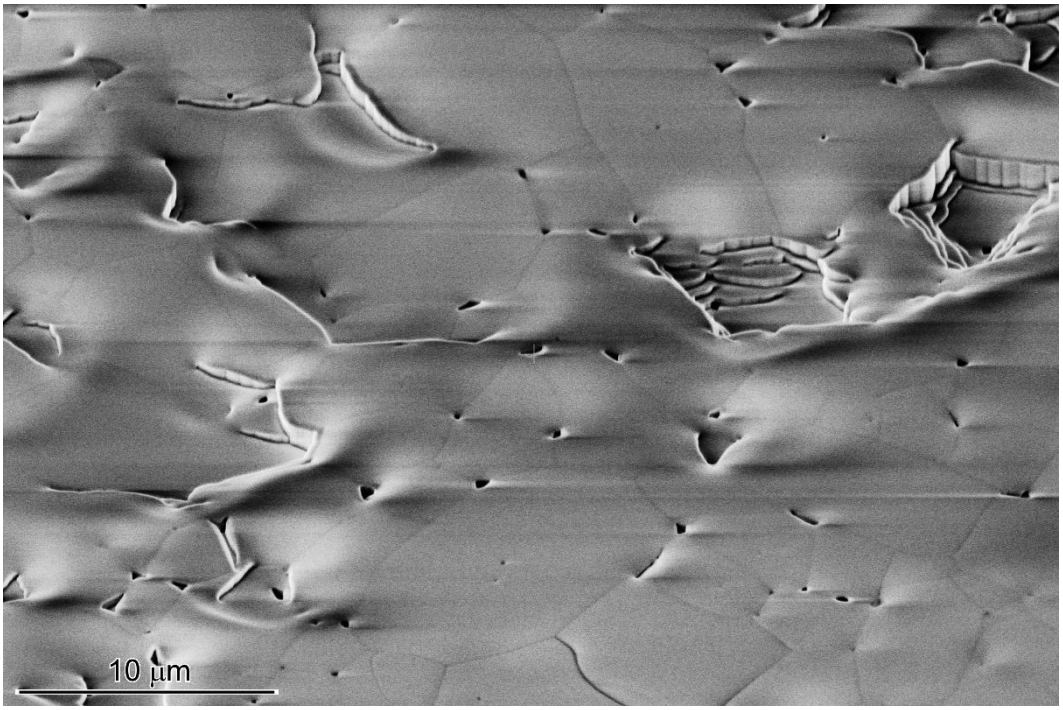

Figure 34: SE SEM micrograph acquired from the dual-beam Xe FIB using incident electrons, from a Ca-doped sample after ion polishing to remove pull-out damage. Ion polishing was done at an incident angle of near 0° and a current of 60 nA.

4.1.2 Actual Concentrations

Since a main part of this work involves examining the influence of increasing the Ca content, it is crucial to ensure that the Ca content is below the solubility limit of Ca at 1600°C (51 ppm [19]) after the sintering process. Dopants intentionally added to the powder or in solution may evaporate during sintering while impurities may enter the material during the processing. Ca, Mg and Si are all commonly found in commercial alumina powders, while Mg and Si are common in our working environment. Si in particular can be introduced to the alumina slips from the furnace's molybdenum disilicide ($MoSi_2$) heating elements during sintering.

In order for the measured concentrations to be meaningful, the concentration limit had to be measured. A reported concentration without a detection limit holds limited value. The detection limits were measured for every element within a specific sample, taking into consideration the operating conditions of the WDS/SEM system on a given day and the number of measurements performed, using equation (15).

The measured Ca, Si and Mg content in our sintered alumina, the detection limits and the starting powder concentration (as provided by the supplier [58]) are presented in Table 2.

Table 2: Summary of the dopant/impurity concentrations in the alumina produced for this study.

	Dopant	**Concentration [ppm]**	**Detection limit [ppm]**	**Initial powder concentration [ppm] [58]**
Undoped alumina	Ca	6 ± 4	3	5
	Si	14 ± 9	9	15
	Mg	8 ± 9	7	5
Ca-doped alumina	Ca	19 ± 4	2	5
	Si	26 ± 11	9	15
	Mg	< Det. limit	7	5

The measurements confirm that the Ca content in our Ca-doped alumina is below the solubility limit in alumina at 1600°C (summarized in Table 1), as are the Si and Mg contents. The Ca, Si and Mg contents in the undoped alumina are roughly equivalent to those of the starting powder. The detection limit for Mg is larger than the manufacturer's reported concentration and is barely detectable in the undoped alumina.

In the Ca-doped alumina, the initial Ca content was increased threefold, from 6 ppm to 19 ppm. No Mg was detected above the detection limit and the Si content was increased from 14 ppm to 26 ppm. This was unintentional and a result of contamination during the processing, likely from the environment of the sintering furnace.

4.2 Grain Growth of Undoped Samples

4.2.1 Conventional Grain Growth

The microstructure of the undoped alumina samples annealed in air at 1600°C for 2, 4, 6 and 8 hours are presented in Figure 35.

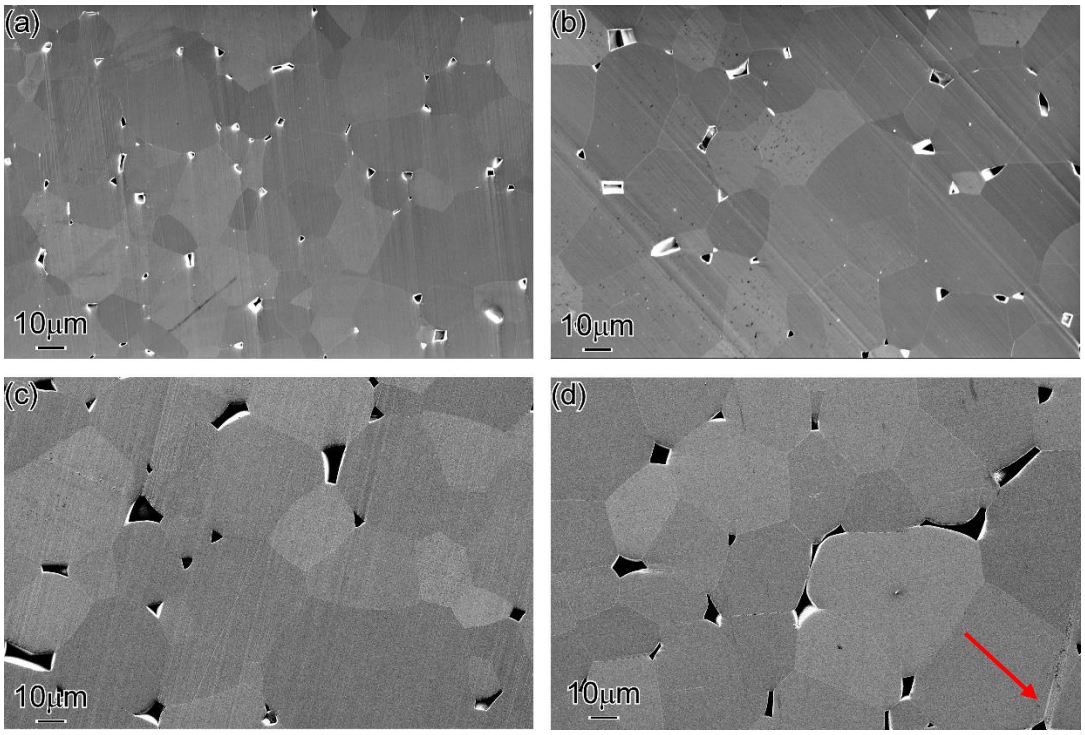

Figure 35: SE SEM micrographs (polished and thermally etched cross-section) of the microstructure of undoped alumina samples annealed in air at 1600°C for (a) 2 hours, (b) 4 hours, (c) 6 hours and (d) 8 hours. The red arrow marks an example for scratching damage caused by a "pulled-out" grain during the polishing process.

The presented micrographs confirm that the grains remain equiaxed after annealing for 8 hours, which is to be expected given the low measured Ca and Si contents presented in Table 2. The red arrow in Figure 35 (d) shows an example for pull-out debris that scratched the sample's surface during polishing.

4.2.2 The Influence of a Field on Grain Growth

The microstructure of the undoped alumina samples annealed in air at 1600°C for 2 and 8 hours under a static electric field of 200 V/cm are presented in Figure 36.

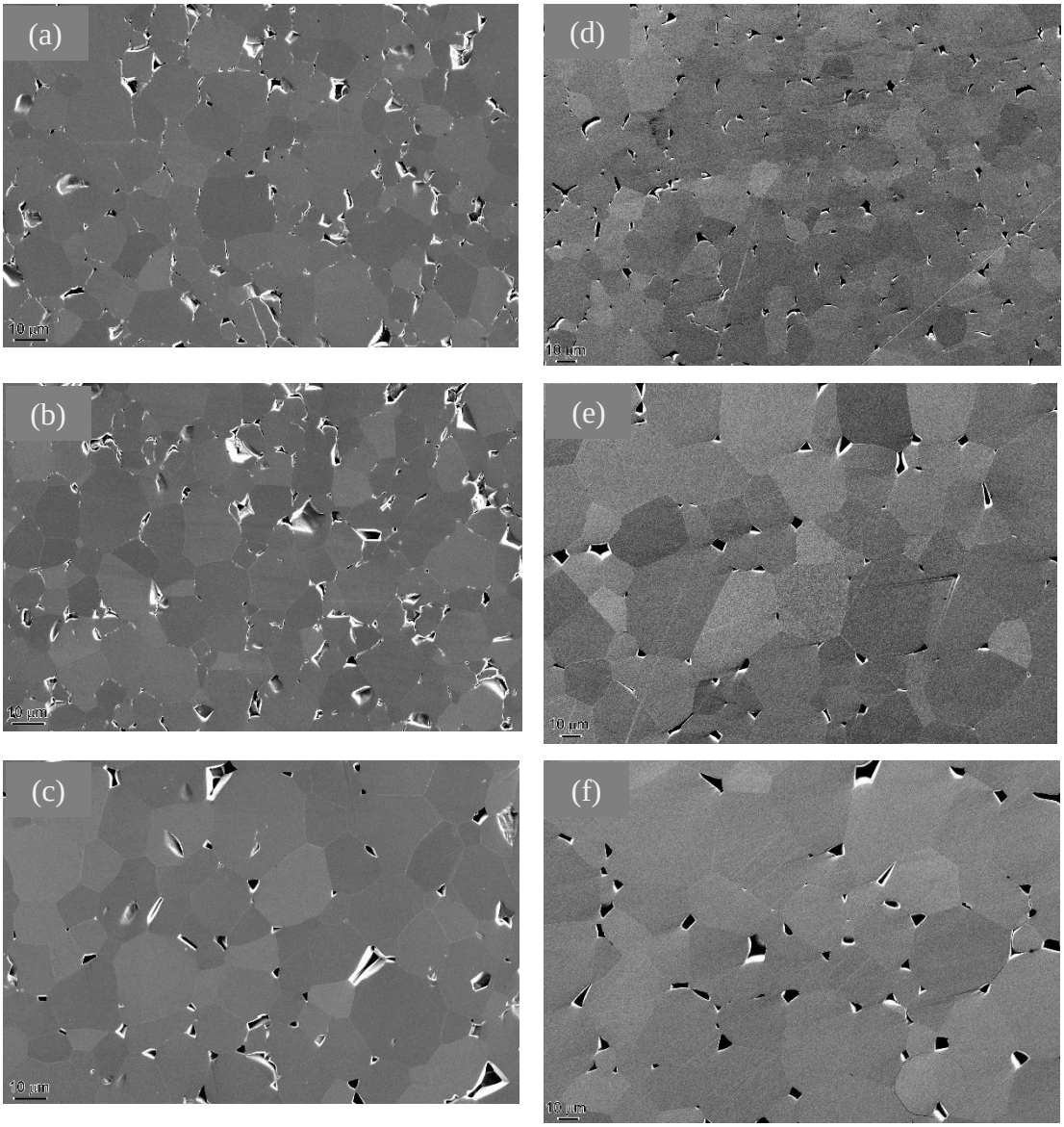

Figure 36: SE SEM micrographs (polished and thermally etched cross-section) of the microstructure of undoped alumina samples annealed in air at 1600°C for (a)-(c) 2 hours and (d)-(f) 8 hours under a static electric field of 200 V/cm: (a) and (d) were taken 100 μm adjacent to the positive electrode, (b) and (e) from the middle of the sample and (c) and (f) 100 μm adjacent to the negative electrode.

The presented microstructures in Figure 36 (a)-(c) show no discernible difference between the areas of the sample adjacent to the positive and negative electrodes, or the middle of the sample, for a short annealing time of 2 hours. For 8 hours, however, as can be seen in Figure 36 (d)-(f), the grain size observed 100 μm adjacent to the positive electrode (d) is considerably smaller than the middle of the sample (e), which is smaller than 100 μm adjacent to the negative electrode (f). This is in line with the findings by Marder et al. [51] using SPS to anneal undoped alumina.

To confirm the difference in the average grain size and calculate the effective grain boundary mobility, the change in the average grain size as a function of time at 1600°C was measured for the samples annealed under the static electric field and those annealed without a field. The grain growth kinetics are shown in Figure 37.

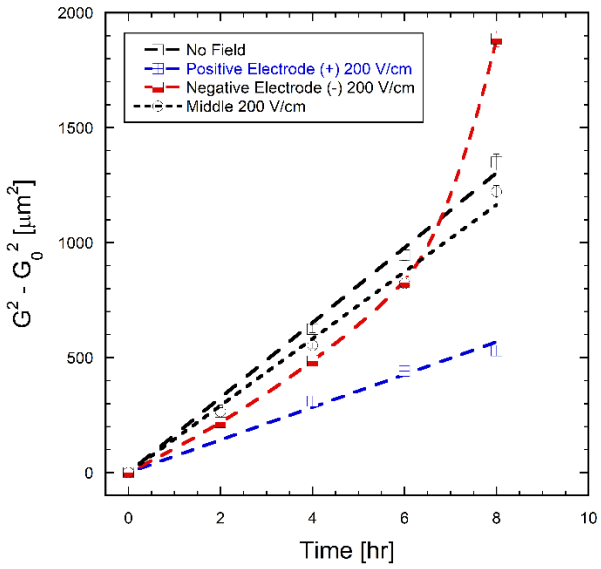

Figure 37: Grain growth kinetics of undoped alumina samples annealed in air at 1600°C without a field and under a static electric field of 200 V/cm.

The effective grain boundary mobilities were determined from the parabolic grain growth kinetics using equation (6). The measured effective grain boundary mobility from these undoped samples are 11.3 (± 0.2)·10^{-15} m^2/sec when annealed without a field, 4.9 (± 0.2)·10^{-15} m^2/sec adjacent to the positive electrode, 10.1 (± 0.3)·10^{-15} m^2/sec at the middle of the sample and 12.9 (± 1.8)·10^{-15} m^2/sec adjacent to the negative electrode.

These results, along with the observed microstructure, confirm that the static electric field causes inhomogeneous grain growth kinetics, similarly to what was observed for alumina annealed in SPS by Marder et al. [51]. The effective grain boundary mobility adjacent to the negative electrode is not considerably higher than that when no field was used during annealing, but it is definitely higher than the mobility measured adjacent to the positive electrode (within the margins of error).

To repeat the experiment and confirm its validity, another set of undoped alumina samples were annealed for similar times and under an increased electric field strength of

300 V/cm. The microstructure of these undoped alumina samples annealed in air at 1600°C for 2 and 8 hours are presented in Figure 38.

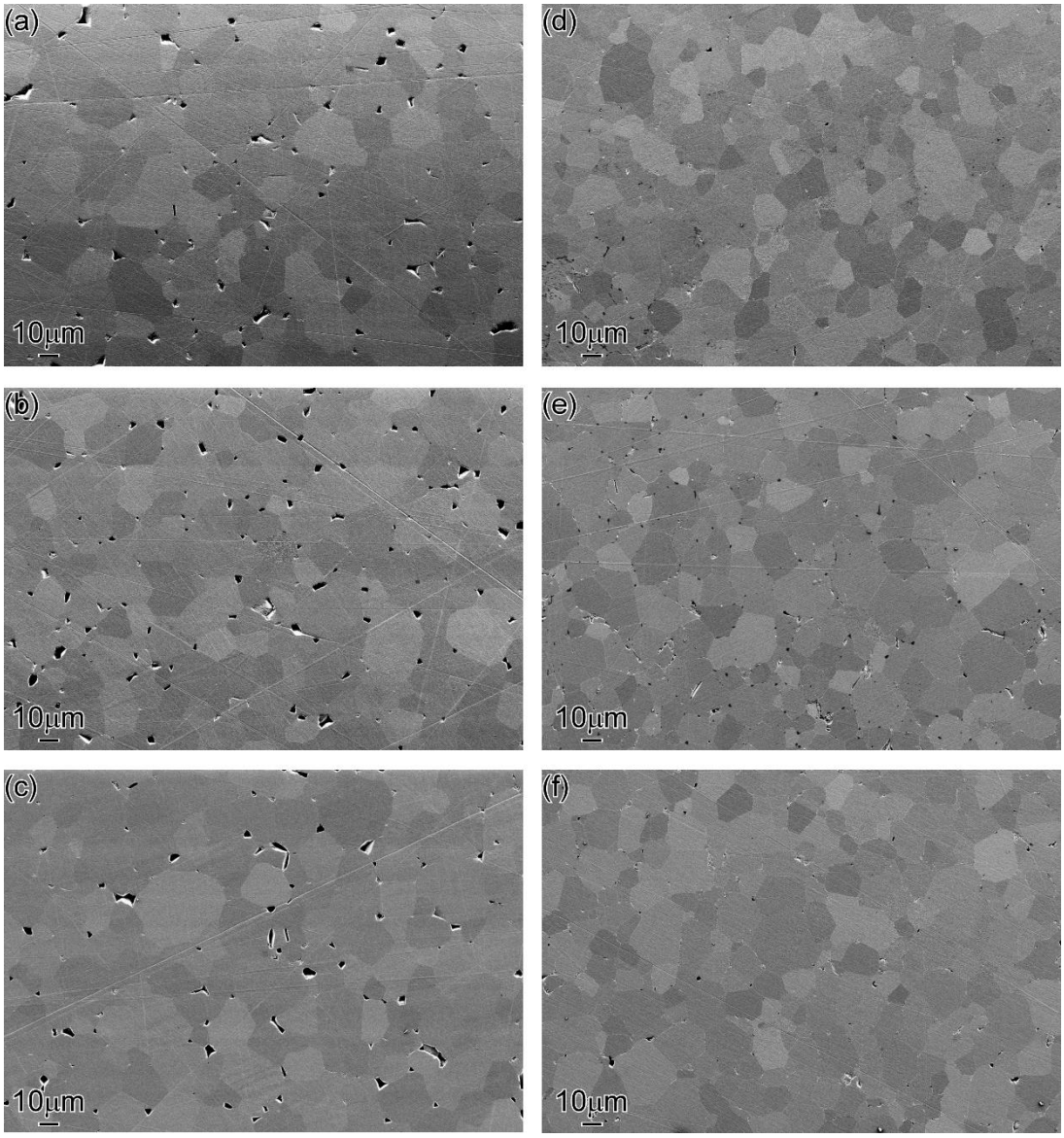

Figure 38: SE SEM micrographs (polished and thermally etched cross-section) of the microstructure of undoped alumina samples annealed in air at 1600°C for (a)-(c) 2 hours and (d)-(f) 8 hours under a static electric field of 300 V/cm: (a) and (d) were taken 100 μm adjacent to the positive electrode, (b) and (e) from the middle of the sample and (c) and (f) 100 μm adjacent to the negative electrode.

Contrary to the microstructures presented in Figure 36, the microstructures presented in Figure 38 (a)-(c) do show a discernible difference between the grain size adjacent to the positive electrode and the negative electrode after as little as 2 hours of annealing. This is in line with what was expected as a result of increasing the strength of the electric field. Similar to when the alumina samples were annealed under a static electric field of

200 V/cm, this trend is maintained when annealing for 8 hours, as can be seen in the microstructures presented in Figure 38 (d)-(f).

The grain growth kinetics of the undoped samples annealed under a static electric field of 300 V/cm are presented in Figure 39.

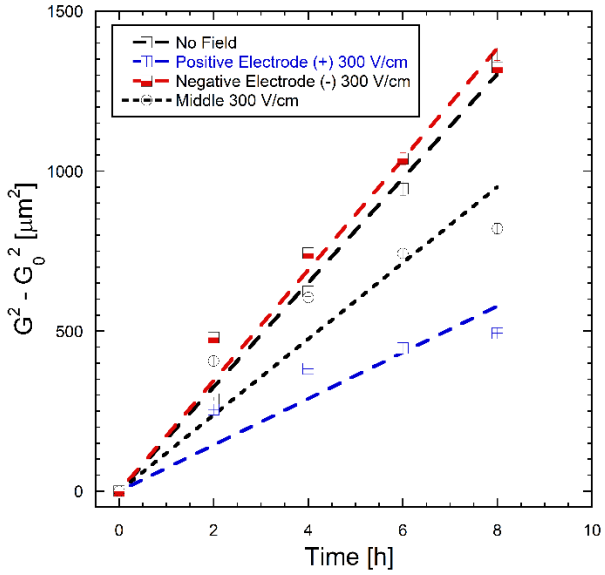

Figure 39: Grain growth kinetics of undoped alumina samples annealed in air at 1600°C without a field and under a static electric field of 300 V/cm.

The effective grain boundary mobilities measured from these undoped samples are 5.0 (± 0.5)·10^{-15} m^2/sec adjacent to the positive electrode, 8.3 (± 0.8)·10^{-15} m^2/sec at the middle and 12.0 (± 0.5)·10^{-15} m^2/sec adjacent to the negative electrode. The general trend and behavior of the grain growth kinetics observed for a static electric field of 200 V/cm were successfully recreated by increasing the field to 300 V/cm.

Considering the possibility of Pt entering the samples because of the physical contact between them and the electrodes, a piece of the sample that was annealed for 8 hours under a field of 300 V/cm was prepared for WDS. This particular sample was the last to be annealed using these electrodes, meaning the Pt paste will have diffused the most into the alumina disks by this point, if at all. Using WDS, no Pt was measured above the detection limit of 4 ppm at the edges of the sample (closest to either electrode), indicating that there should be no considerable Pt contents 100 μm adjacent to the electrodes where the average grain sizes were measured.

We expected a stronger static electric field to result in a higher effective grain boundary mobility adjacent to the negative electrode. While this seemed to be the case when looking at the average grain sizes alone for t = 2, 4 and 6 hours, the average grain size for t = 8 hours was smaller for 300 V/cm, as is shown in Figure 40:

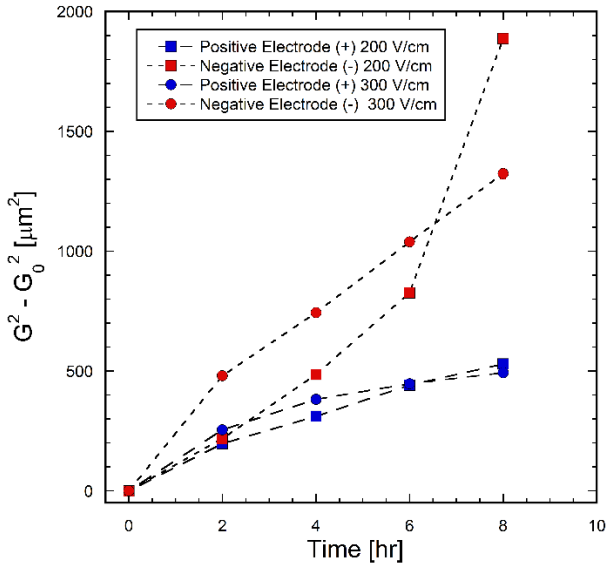

Figure 40: Comparison of the grain growth kinetics presented in Figure 37 and Figure 39.

As a result of this apparent outlier at t = 8 hours for 200 V/cm, the effective grain boundary mobility for 200 V/cm adjacent to the negative electrode (12.9 [± 1.8]·10^{-15} m^2/sec) was higher than for 300 V/cm (12.0 [± 0.5]·10^{-15} m^2/sec).

It is important to point out that as we continued to use the electrodes, a physical deformation was observed, particularly in the positive electrode (presented in Figure 41). The more we continued to use the electrodes, the more drastic the deformation became. This deformation is likely the result of the differing thermal expansion coefficients of the alumina disks and the platinum paste & wires.

Figure 41: Photographs of the physical deformation observed in the positive electrode after using it for all of the aforementioned annealing treatments. A convex shape can be seen where the samples are normally in contact with the electrode. The outwards side of the electrode (coated with Pt paste) is curved inwards, and the layer of Pt paste is no longer uniform, particularly where the wire was brazed to the disk.

The strength of the electric field was taken as the applied voltage divided by the width of the electrodes and the samples. The intention was for the electrodes to be parallel to one another. This deformation would cause the field to stop being uniform throughout the entire sample. The field was at its strongest at the point where the positive electrode is in contact with the sample and weaker elsewhere.

Because of the deformation of the electrodes with time, the lines of the electric field were likely no longer perpendicular to the sample. This could explain the lower average grain size despite having a stronger total applied voltage, especially because of the challenge of managing to always measure the grain size from where the field was the highest.

Another possible explanation is that this lack of uniformity in the field potential is the reason the average grain size after t = 8 hours and a field of 200 V/cm is larger compared to samples after annealing at 300 V/cm. Overall, this is a limitation of the experimental system. When omitting the data point of 8 hours under a field of 200 V/cm adjacent to the negative electrode, the mobility goes down to $9.1\ (\pm\ 0.4)\cdot 10^{-15}\ m^2/sec$.

Because of the deformation of the electrodes, a new pair was fabricated for use with the Ca-doped samples.

4.3 Grain Growth of Ca-Doped Samples

4.3.1 Conventional Grain Growth

The microstructure of the Ca-doped alumina samples annealed in air at 1600°C for 2, 4, 6 and 8 hours are presented in Figure 42, with damage from polishing being especially apparent for t = 6 and 8 hours.

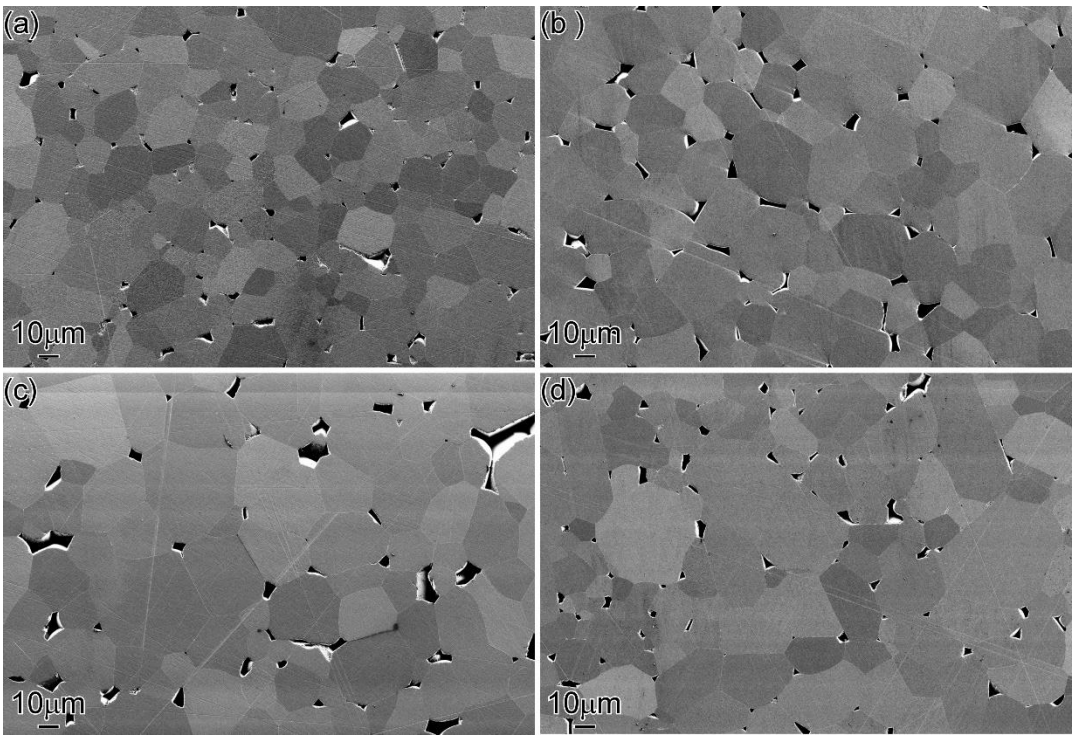

Figure 42: SE SEM micrographs (polished and thermally etched cross-section) of the microstructure of Ca-doped alumina samples annealed in air at 1600°C for (a) 2 hours, (b) 4 hours, (c) 6 hours and (d) 8 hours.

It should be noted that, while some grains seem to indicate the beginning of elongated grain growth, the microstructure after 8 hours appears to still be mostly equiaxed.

4.3.2 The Influence of a Field on Grain Growth

After a new pair of electrodes were fabricated, a similar set of annealing treatments under a static electric field of 300 V/cm was performed. The microstructures for 2 and 8 hours are presented in Figure 43.

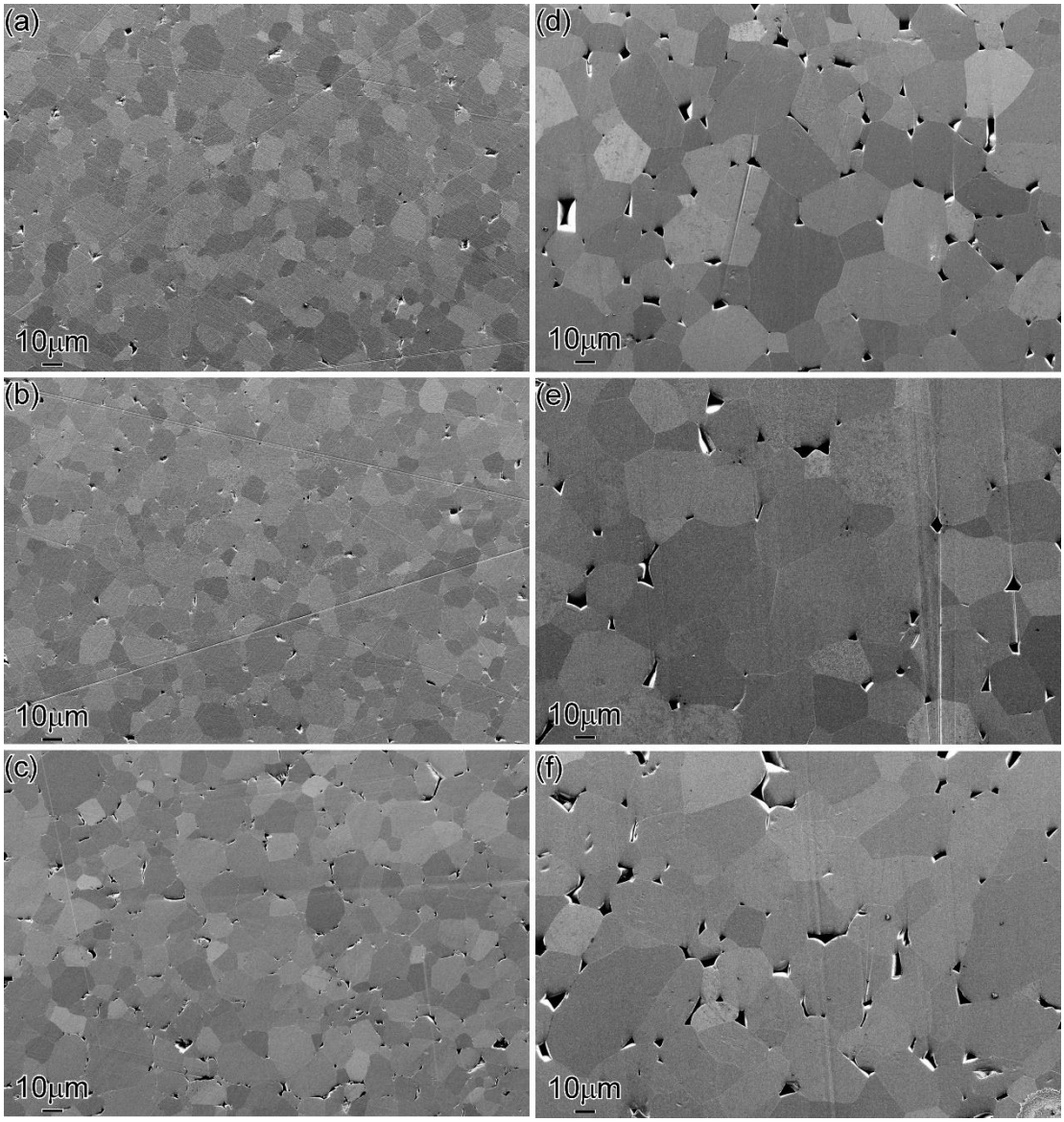

Figure 43: SE SEM micrographs (polished and thermally etched cross-section) of the microstructure of Ca-doped alumina samples annealed in air at 1600°C for (a)-(c) 2 hours and (d)-(f) 8 hours under a static electric field of 300 V/cm: (a) and (d) were taken 100 μm adjacent to the positive electrode, (b) and (e) from the middle of the sample and (c) and (f) 100 μm adjacent to the negative electrode.

In the presented micrographs, a difference between the positive and negative electrode is not immediately evident after 2 hours. It is evident after 8 hours, however, and is easily discerned from the grain growth kinetics in Figure 44, which includes over 700 grains for each data point. It is noteworthy that signs of the beginning of elongated grain growth are more prominent here than when the annealing was done without a field, and that these grains are mostly "pointing towards" the electrodes (the top/bottom of the micrographs).

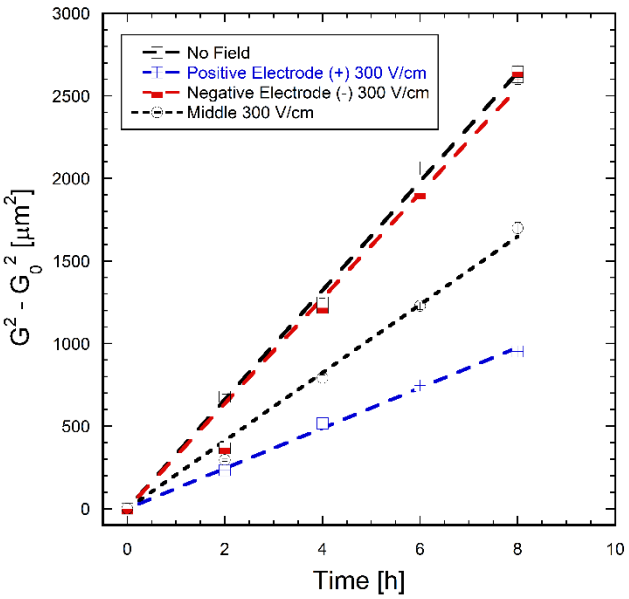

Figure 44: Grain growth kinetics of Ca-doped alumina samples annealed in air at 1600°C without a field and under a static field of 300 V/cm.

The effective grain boundary mobilities measured from these Ca-doped samples are 22.9 (± 0.3)·10^{-15} m^2/sec when annealed without a field, 8.5 (± 0.1)·10^{-15} m^2/sec adjacent to the positive electrode, 14.3 (± 0.4)·10^{-15} m^2/sec at the middle and 22.1 (± 0.9)·10^{-15} m^2/sec adjacent to the negative electrode.

All of the effective grain boundary mobilities measured in this study are summarized in Table 3, and a comparison between undoped and Ca-doped alumina is presented in Figure 45.

Table 3: Summary and comparison of the effective grain boundary mobilities measured from the undoped and Ca-doped alumina samples.

		Effective GB Mobility 10^{-15} $\left[\frac{m^2}{sec}\right]$	
		Undoped alumina	**Ca-doped alumina**
No Field		11.3 ± 0.2	22.9 ± 0.3
300 V/cm	**Positive electrode**	5.0 ± 0.5	8.5 ± 0.1
	Middle	8.3 ± 0.8	14.3 ± 0.4
	Negative electrode	12.0 ± 0.5	22.1 ± 0.9
200 V/cm	**Positive electrode**	4.9 ± 0.2	-
	Middle	10.1 ± 0.3	-
	Negative electrode	9.1 ± 0.4 (omitting 8 hours)	-

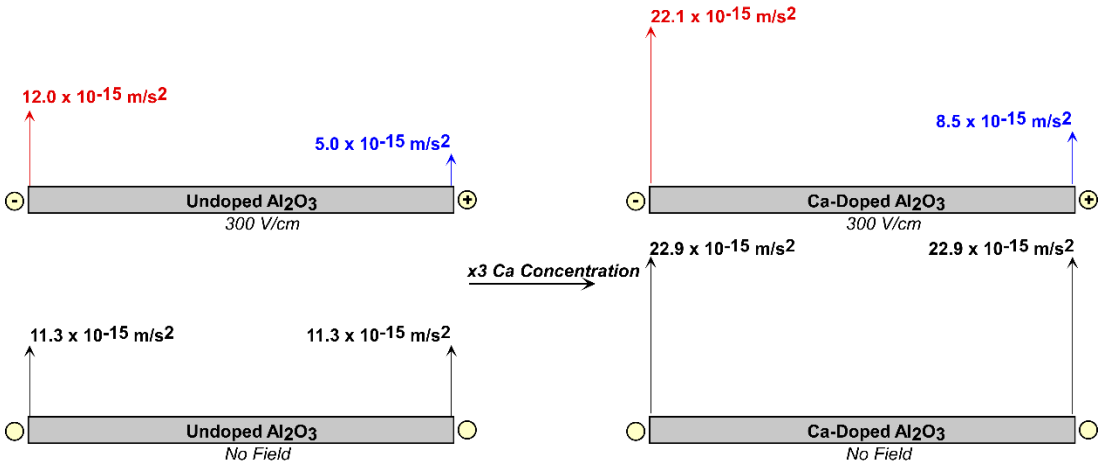

Figure 45: Summary and comparison of the results for undoped and Ca-doped alumina annealed without an electric field and under a field of 300 V/cm.

The addition of Ca to alumina via ***intentional*** doping, as was observed in previous studies, does lead to an ***increase*** in the effective GB mobility. This is in line with what has been demonstrated in previous works, most importantly those where it was confirmed that the Ca contents were below the solubility limit of Ca in alumina [20,34].

Once again, as was the case in the undoped alumina, the field caused inhomogeneous grain growth kinetics, with the effective grain boundary mobility being the highest adjacent to the negative electrode.

4.3.3 Solute Distribution and Fields

Measuring the concentration of oxygen vacancies, or rather the lack of oxygen, is challenging. Therefore, to try and begin to examine our hypothesis regarding the role of oxygen vacancies in facilitating grain growth, the Ca-doped sample annealed in air at 1600°C under a static electric field of 300 V/cm for 8 hours was taken for WDS measurements. The Ca content was measured as a function of distance from the negative electrode. The sample was 2.88 mm thick and the results are summarized in Figure 46 and Table 4.

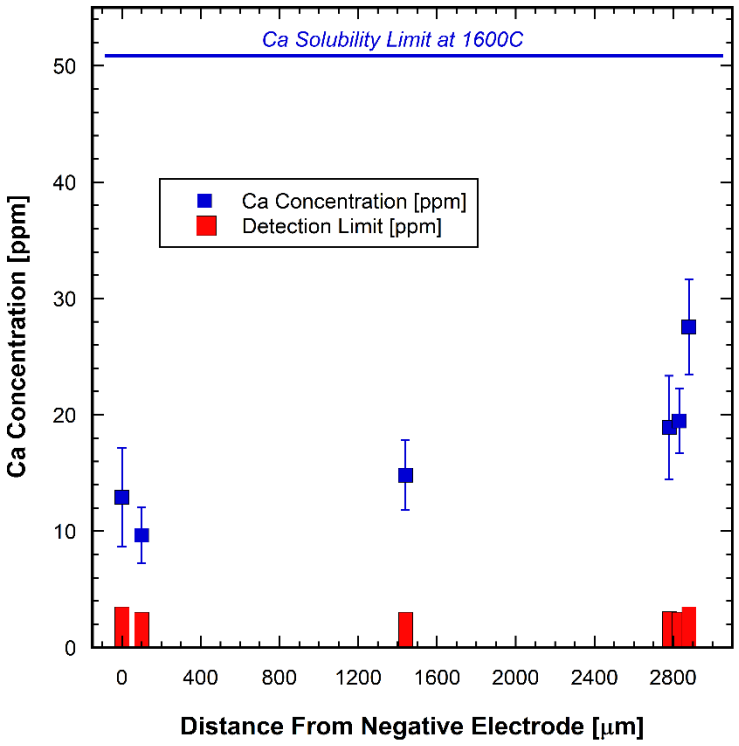

Figure 46: The measured local Ca concentrations after annealing a Ca-doped sample for 8 hours under a static electric field of 300 V/cm, as a function of distance from the negative electrode. The X-axis is the distance from the negative electrode. The detection limits for each measurement and the solubility limit of Ca at 1600°C are displayed as well.

Table 4: Summary of the measured local Ca concentration and corresponding detection limits presented in Figure 46.

Distance from the negative electrode [μm]	Measured Ca concentration [ppm]	Detection limit [ppm]
0	13 ± 12	4
100	10 ± 7	3
1440	15 ± 8	3
2780	19 ± 12	3
2830	19 ± 8	3
2880	28 ± 11	4

The concept behind making these measurements was that if the oxygen vacancies are attracted towards the negative electrode, one could expect the Ca cations to gradually diffuse towards the positive electrode. These results do confirm this hypothesis for Ca, and the interesting aspect is that a ***higher*** local Ca concentration is now directly correlated with a ***lower*** effective grain boundary mobility. This contradicts measured mobilities from Ca doped samples without an applied electric field [20,21,34,45].

The effective grain boundary mobility 100 μm adjacent to the negative electrode, where a local Ca concentration of 10 ppm was measured, is 22.1 (± 0.9)·10^{-15} m^2/sec. It is considerably higher than 100 μm adjacent to the positive electrode, 8.5 ± 0.1·10^{-15} m^2/sec, where a local Ca concentration of 19 ppm was measured. Equally important, the mobility adjacent to the positive electrode is now lower than that of the undoped alumina, 11.3 (± 0.2)·10^{-15} m^2/sec, and the Ca concentration in the undoped alumina is 6 ppm.

5. Discussion

5.1 Ca and Conventional Grain Growth

In this work, we experimentally confirm that doping alumina with Ca results in an increase in the effective grain boundary mobility. This confirms past works, many of which never confirmed the actual Ca concentrations in their samples [18,36,37,38], as well as those where the concentrations were measured. Akiva et al. and Moshe et al. also reported an increase in the effective grain boundary mobility as a result of doping alumina with Ca. Their TEM analysis also demonstrated that Ca at concentrations below the solubility limit segregates to GBs in alumina [20,34].

This contrasts with Mg doping, which also segregates to GBs in alumina but *reduces* the effective grain boundary mobility [18,29,30,31,32,34] as a result of the solute-drag effect [17]. Baik and Moon demonstrated this as well, and suggested that Mg cations play a beneficial role in controlling the anisotropic segregation of Ca cations to the GBs [35].

Another work by Moshe et al. investigated the effect of co-doping alumina with Mg and Ca [66]. They demonstrated that oversaturating alumina with both dopants to a level above their previously known solubility limits at 1600°C has an impact on the solubility limits of each dopant. Using quantitative WDS analysis, they determined the solubility limits to be 210 ± 43 ppm for Mg and 32 ± 13 ppm for Ca. These values represent an increase from the 132 ± 11 ppm reported by Miller et al. for Mg, and a decrease from the 51 ± 1 ppm reported by Akiva et al. for Ca, when alumina was doped with only one of the elements [33,19].

When co-doping alumina below these aforementioned solubility limits, Moshe et al. demonstrated a decrease in the effective grain boundary mobility, indicating that solute-drag due to the segregation of Mg to the GBs is dominant over the solute-acceleration due to Ca segregation [66].

Dillon and Harmer claimed that the increase in the mobility, resulting from Ca segregation, is due to a first order complexion transition at the grain boundary (presented

in Figure 47), altering the structure and/or chemical composition of the GBs [18]. While this transition may result in an increased mobility, it does not explain how the mechanism for grain boundary movement is affected.

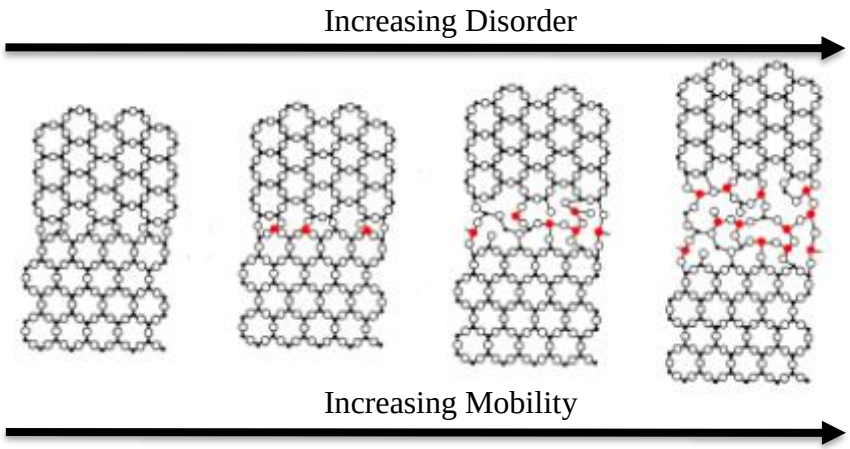

Figure 47: Schematic of the effect of increasing disorder within the core of a grain boundary on the grain boundary mobility; reproduced from [18].

Disconnections at the GBs have been demonstrated to be the main mechanism by which GBs move [9,10,11,12,13]. Simulations have been used to show that GB migration occurs through the nucleation and motion of disconnections [14], and the role of disconnections in grain growth has been extensively modeled [15].

Figure 48 presents a schematic drawing of Gibbsian segregation to a high angle grain boundary. It schematically describes how segregation results in a change in the composition of the grain boundary and potentially a change in the 2D structure, showing the formation of additional types of disconnections. The presence of additional types of disconnections indicates that solute segregation might ***decrease*** the activation energy required to create them, which is in line with the modelling done by Han et al. [15].

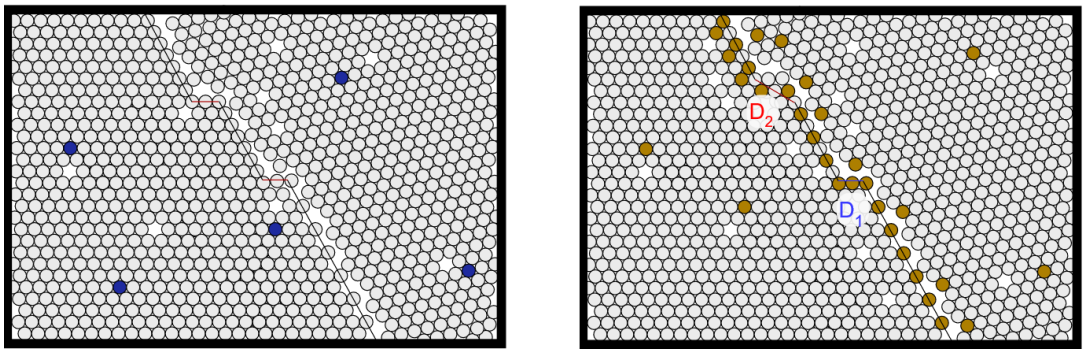

Figure 48: Schematic drawing of a general grain boundary in a polycrystalline matrix. One type of disconnection is presented when there is no segregation, and an additional type of disconnection is formed when segregation occurs.

For the case of solute-drag, as is the case with Mg in alumina for example, Mg segregates to the GBs and potentially ***increases*** the activation energy required to create some types of disconnections, causing there to be less disconnections at the GBs and reducing the grain boundary mobility. When it comes to Ca, however, the segregation may result in the opposite effect; ***decreasing*** the activation energy required to create additional types of disconnections and thus increasing the grain boundary mobility.

Similarly, the segregation of solutes to GBs can make existing disconnections move slower/faster [67]. In the case of Mg in alumina, the segregation to the GBs at a concentration below the solubility limit might hinder the movement of existing disconnections in the planes of the GBs, whereas Ca segregation might lead to an increase in the lateral movement of the disconnections in the planes of the GBs. The change in activation energy, or mobility of existing disconnections, is offered as a plausible mechanism for solute-drag, but has not been experimentally proven.

Several works have used computational methods to determine the energetically preferable charge compensating defects for Mg and Ca in alumina [68,69,70]. For Ca, the charge compensation is carried out by generating oxygen vacancies for divalent ion substitution (e.g. Ca^{2+} replacing Al^{3+}). This results in an effective charge of -1 on the Ca and +2 on the oxygen vacancies.

$$2CaO \leftrightarrow \quad 2Ca'_{Al} + V_O^{\cdot\cdot} + O_O^x \qquad (16)$$

For Mg, the accepted charge compensating defect is self-compensation by Mg interstitials for divalent ion substitution, likely due to the smaller cation size [68,69,70].

$$3MgO \leftrightarrow \ 2Mg'_{Al} + Mg_i^{\cdot\cdot} + 3O_O^x \qquad (17)$$

Mg is known to decrease the grain boundary mobility via solute-drag. This may be the result of the self-compensating Mg interstitials hindering the motion of existing disconnections by pinning them and/or increasing the activation energy to form additional disconnections.

In comparison, an increase in the amount of oxygen vacancies adjacent to the GBs as a result of doping with Ca, which presumably affects the chemical composition and/or structure of the disconnections at the GBs, could be the cause for the decrease in the activation energy required to create more disconnections and/or increasing the mobility of existing disconnections. Previous works have not demonstrated whether or not the oxygen vacancies are directly responsible for this increase in the grain boundary mobility, and here we used an electric field in our annealing treatments to attempt to address this question.

5.2 The Influence of Electrical Fields on Grain Growth

5.2.1 Fields Can Influence Mobility

This work demonstrated an increase in the effective grain boundary mobility as a result of Ca-doping and a decrease in the effective grain boundary mobility adjacent to the positive electrode when applying a static electric field during annealing. A similar behavior was also demonstrated for alumina annealed using SPS [51]. This should be considered when employing electric fields for sintering, i.e. ***electric fields do change grain growth kinetics***.

The work carried out on alumina by Jeong et al. involved a similar system to the one used in this research and showed a clear influence of the direction of the applied static electric field on the mobility of GBs [52]. However, the results for our Ca-doped alumina annealed at under a field of 300 V/cm for 8 hours, presented in Figure 43 (d) and (f), do

not clearly indicate anisotropic grain growth in either the parallel or perpendicular directions with respect to the electric field.

They attempted to use the space-charge at GBs to explain the mechanism through which the electric field influences the grain boundary mobility, by examining the activation energy required for ions to cross from a small grain to the adjacent larger one, which is presented in Figure 49 considering a positively charged grain boundary core. ΔG_d is the capillary driving force. When the grain boundary core is positively charged, the activation energy for an ionic cation jump (ΔG_c) will be higher than for an ionic anion jump (ΔG_a).

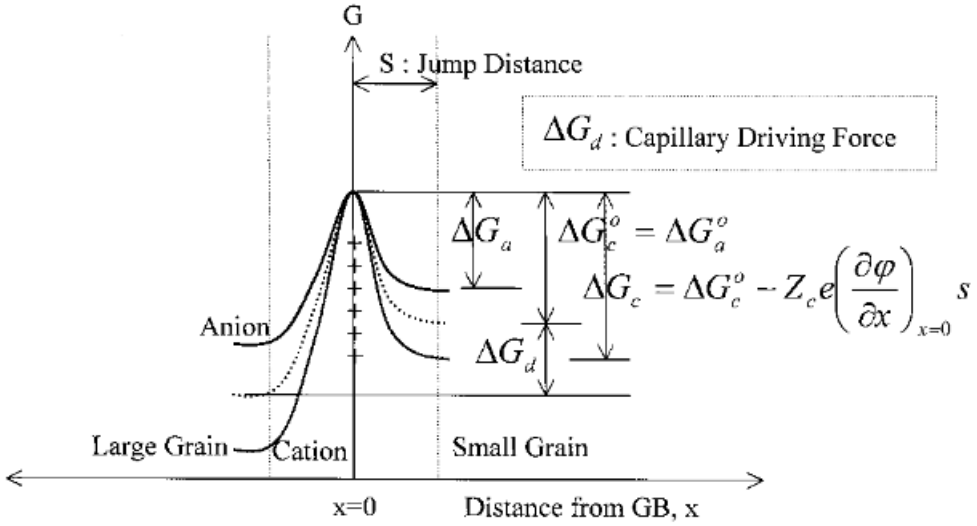

Figure 49: Schematic illustration of the effect of the grain-boundary charge on the activation energy for an ionic jump; reproduced from [52].

They estimated the change in the activation energy for an ionic species *i*, due to the grain boundary charge, by the following relation:

$$\Delta G_i = -Z_i e\left(\frac{\partial \varphi}{\partial x}\right)_{x=0} s \qquad (18)$$

where Z_i is the valence charge of the ion, e is the charge of an electron, s is the jump distance of the ion and $(\partial\varphi/\partial x)_{x=0}$ is the gradient of the electrostatic potential that is generated by the charges at the grain boundary.

The change in the activation energy when a bias *v* is applied is presented in Figure 50, and described by the following equation:

$$\Delta G_i = \Delta G_i^0 - Z_i e\left(\frac{\partial(\varphi + v)}{\partial x}\right)_{x=0} s \qquad (19)$$

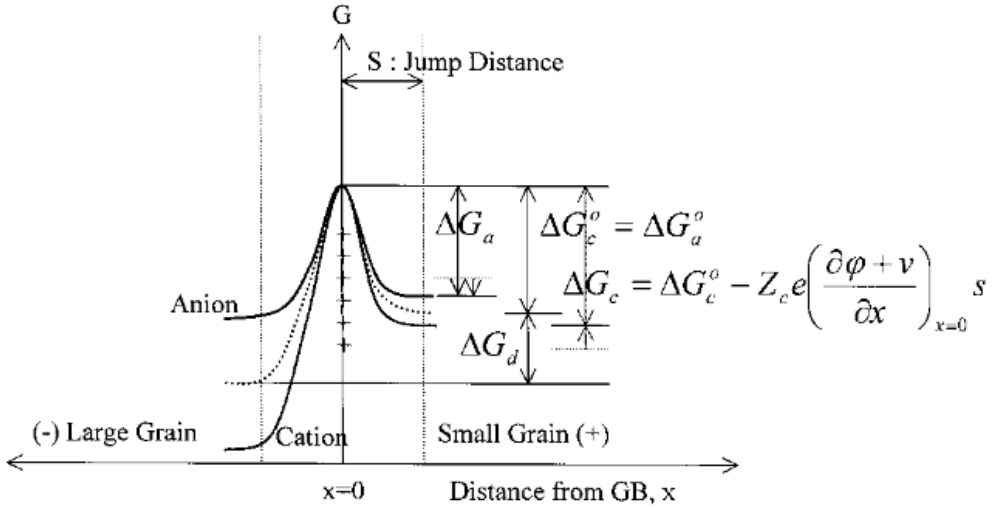

Figure 50: Schematic illustration of the effect of an applied bias on the activation energy for an ionic jump; reproduced from [52].

When a positive bias is applied to the small-grained region of their samples, cations are driven towards the large-grained cathode side and anions are driven towards the small-grained anode side. As a result ΔG_c, which is higher than ΔG_a, is decreased, while ΔG_a is increased. Therefore, the overall rate of ionic jumps increases and the grain boundary migration rate increases.

Using an approximation for the spatial variation of the electrostatic potential, the Debye length and by assuming that the potential of the grain boundary can be described with an exponentially decaying function, Jeong et al. described the change in the Gibbs free energy caused by an ionic jump across the grain boundary. It can be seen in Figure 51 and described using:

$$\Delta G_m = \Delta G_d + Z_c e\left(\frac{v}{X_D}\right)_{x=0} s \qquad (20)$$

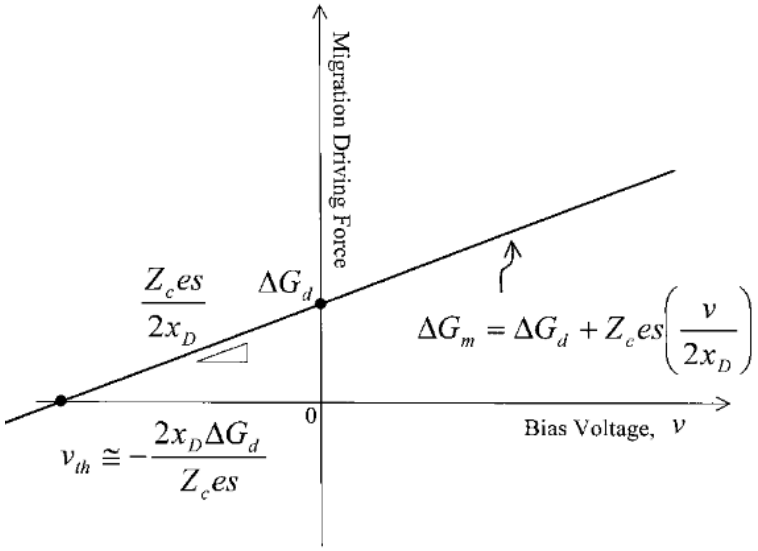

Figure 51: The change in the driving force for grain-boundary migration as a function of an applied bias voltage *v*; reproduced from [52].

As such, the grain boundary migration is expected to be halted entirely when a specific threshold voltage (v_{th}) is applied. By assuming a grain-boundary energy of 1 J/m^2, the two different grain sizes measured prior to the annealing experiment under the static electric field (~170 μm and ~4 μm for the large-grained and small-grained region respectively), $Z_c = 3$, s = 2 Å and X_D = 10 nm, v_{th} was deduced to be 1075 V, applied to the large-grained region of the sample. The voltage Jeong et al. applied during their experiments was 200 V, which is much lower than this estimated threshold, but the concept of potentially halting the migration of a grain boundary with a strong enough perpendicular static electric field is worth exploring further.

While the work by Jeong et al. is in line with other works demonstrating the influence of an electric field of grain growth in general [53,54,57] and this present study in particular, it leaves a lot to be desired. While the influence of the electric field is unquestionable and space-charge may indeed play a role in the mechanism of grain boundary motion, their proposed mechanism is overly simplistic. When the effective GB mobility is associated with a space-charge at the GB, the application of an electric field should result in an anisotropic microstructure, which was not clearly demonstrated in this work. The model suggests that ions merely find it easier or harder to "jump" across the grain boundary, without addressing the role of disconnections. Does the space-charge facilitate the nucleation of disconnections, their motion, or both?

Equally important, Jeong et al. did not measure the dopant/impurity content of their samples, and looked solely at the migration distance of the GB into the small-grained region (ΔL), at the center of their samples for a single annealing time of 2 hours, whereas a series of different annealing times would have provided a clearer trend and allowed for effective GB mobility measurements.

The average grain sizes were only measured prior to the annealing treatment. Since the motion of GBs is directly correlated to the size of grains at a given time, measuring the average grain size again is vital. In particular, it would have been interesting to look the grain growth rates in both the small-grained and large-grained regions of their samples adjacent to the electrodes as a function of time depending on the direction of the field.

For example, when Akiva et al. measured the effective mobility of the (0001) plane of sapphire by diffusion bonding it to alumina, performing annealing treatments and measuring ΔL as a function of time [34], the following equation was used, ***based on equation (6)***:

$$\overline{\Delta L}(t) = 2M_S\gamma_{GB}\frac{\sqrt{k_1 t + \overline{G}_0^{\,2}} - \overline{G}_0}{k_1} \tag{21}$$

where M_S is the (0001) single crystal GB mobility, $\overline{G}_0$ is the initial average grain size of the polycrystalline region the single crystal grows into and k_1 is the same grain growth constant from equation (6), meaning the average grain size at t = 0 and at any given annealing time must be taken into consideration.

The results of the application of the static electric field in this work coincides with the work by Marder et al. [51], showing a decrease in the effective GB mobility adjacent to the positive electrode. However, the field in SPS in undefined due to the short circuit in the system. Additionally, sintering and annealing in SPS are done in an environment that is carbon-rich and has a low partial pressure of oxygen, $P(O_2)$. Carbon has been shown to result in a reduced GB mobility in alumina [71] and a low $P(O_2)$ influences the amount of oxygen vacancies in the samples.

While the lower $P(O_2)$ and consequently the higher concentration of oxygen vacancies in the alumina annealed in SPS may help explain why the effective mobility measured by Marder et al. ($27.0 \pm 2.0 \cdot 10^{-15}$ m^2/sec) is higher than that measured in this work ($11.3 \pm 0.2 \cdot 10^{-15}$ m^2/sec), despite carbon doping, several factors complicate direct comparison. These include the undefined field, as well as variations in carbon and other impurity concentrations between the two studies.

Once again, we return to the issue of oxygen vacancies. Although WDS cannot be used to measure their concentration directly, we did observe variations in local Ca concentrations.

5.2.2 Separation of Ca and Oxygen Vacancies

The intentional doping of alumina with Ca and the use of an external electric field can be compared with one another. The measured effective GB mobility increases as a result of Ca doping and decreases adjacent to the positive electrode as a result of applying the external electric field. the common denominator is the respective increase and decrease in the concentration of oxygen vacancies. A possible explanation for the effective mobility not further increasing adjacent to the negative electrode is that the GBs are already saturated with oxygen vacancies, or that further increase in the concentration of oxygen vacancies is inconsequential.

Our WDS measurements presented in Figure 46 and Table 4 ***confirmed a change in the local Ca concentration*** as a result of applying an electric field of 300 V/cm for 8 hours on a Ca-doped alumina sample. A higher Ca concentration was measured 100 μm from the positive electrode (19 ± 12 ppm) compared to 100 μm from the negative electrode (10 ± 7 ppm). At the very edge of the sample near the positive electrode, the Ca concentration was even higher (28 ± 11 ppm), whereas at the opposite edge of the sample, it was 13 ± 12 ppm.

Since the electric field can separate the Ca cations from their charge compensating oxygen vacancies, it is reasonable to expect the positive electrode to ***repel the oxygen vacancies*** while ***attracting the Ca cations***, and the negative electrode to ***attract the oxygen vacancies*** and ***repel the Ca cations***.

5.2.3 Role of Ca vs Oxygen Vacancies in Influencing Mobility

In the Ca-doped alumina annealed under an electric field of 300 V/cm for 8 hours, a ***higher local Ca concentration*** (19 ± 12 ppm) was measured adjacent to the positive electrode, where a ***lower effective GB mobility*** was measured. Meanwhile a ***higher effective GB mobility*** was measured adjacent to the negative electrode, which coincides with a ***lower local Ca concentration*** (10 ± 7 ppm). Similarly, in our undoped alumina, where the Ca concentration was lower (6 ± 4 ppm), the ***effective GB mobility was higher*** than that measured 100 μm adjacent to the positive electrode in the Ca-doped sample.

In another study on $SrTiO_3$, Qu et al. used electron energy-loss and X-ray photoelectron spectroscopies to experimentally and logically infer a higher oxygen vacancy concentration at the negative electrode from their XPS data [72], correlating it to the increased grain growth rates observed in other works [53,54].

Before drawing conclusions, let us consider the amount of intrinsic oxygen vacancies present in undoped, "pure" alumina (sapphire) at 1600°C. Assuming hypothetically pure sapphire, Lagerlöf and Grimes estimated an intrinsic oxygen vacancy concentration of $\sim 2.6 \cdot 10^{-14}$ ppm at 1600°C [69]. One oxygen vacancy is generated for every 2 Ca cations in the sample, as per equation (16). This helps puts the concentration of oxygen vacancies in our samples (doped and undoped) into perspective. Even the undoped alumina, containing 6 ppm of calcium, has a concentration of oxygen vacancies ***higher by over a dozen orders of magnitude*** compared to pure alumina. Since the intrinsic oxygen vacancy concentration is negligible in comparison to that generated by doping with Ca, increasing the Ca concentration threefold (19 ppm) also increased the concentration of oxygen vacancies threefold.

It has been demonstrated in several works that ***doping alumina with Ca*** leads to an increase in the GB mobility [34,35,36,37,38]. The WDS results shown in Figure 46 indicate that ***Ca causes the more traditional solute-drag effect***, and it can be inferred that the ***oxygen vacancies cause the observed increase in GB mobility***. The increase in GB mobility caused by the oxygen vacancies is more dominant than the solute-drag

caused by the Ca cations, so there is a net increase in GB mobility when alumina is doped with Ca.

6. Summary and Conclusions

The goals of this study were to validate the influence of an electric field on grain growth by measuring the effective GB mobility in undoped and Ca-doped alumina annealed with and without the application of an external static DC electric field, and to correlate it to the change in the local dopant/impurity concentrations.

Undoped and Ca-doped (6 and 19 ppm respectively) polycrystalline alumina samples were prepared. Full densities and low contents of impurities were confirmed using Archimedes' method, a dual-beam Xe FIB and WDS measurements. The samples were thermally annealed in air at 1600°C, for different time durations, with and without the simultaneous application of an external static electric field, and the grain growth kinetics were studied.

The results show that ***doping alumina with Ca causes the effective GB mobility to increase***, which is in line with past works. The calculated effective GB mobilities are $11.3 \pm 0.2 \cdot 10^{-15}$ m^2/sec and $22.9 \pm 0.3 \cdot 10^{-15}$ m^2/sec for the undoped and Ca-doped alumina respectively.

An decrease in the effective GB mobility was also demonstrated near the positive electrode, compared to the rest of the sample, when the samples were annealed under a static electric field. For the undoped alumina annealed under a field of 200 V/cm, the effective GB mobilities measured are $4.9 (\pm 0.2) \cdot 10^{-15}$ m^2/sec 100 μm adjacent to the positive electrode, $10.1 (\pm 0.3) \cdot 10^{-15}$ m^2/sec at the middle of the sample and $9.1 (\pm 0.4) \cdot 10^{-15}$ m^2/sec 100 μm adjacent to the negative electrode.

When the strength of the field was increased to 300 V/cm, the effective GB mobilities measured are $5.0 (\pm 0.5) \cdot 10^{-15}$ m^2/sec 100 μm adjacent to the positive electrode, $8.3 (\pm 0.8) \cdot 10^{-15}$ m^2/sec at the middle of the sample and $12.0 (\pm 0.5) \cdot 10^{-15}$ m^2/sec 100 μm adjacent to the negative electrode.

For the Ca-doped alumina annealed under a field of 300 V/cm, the effective GB mobilities measured are 8.5 ($\pm$ 0.1)$\cdot 10^{-15}$ m^2/sec adjacent to the positive electrode, 14.3 ($\pm$ 0.4)$\cdot 10^{-15}$ m^2/sec in the middle of the sample and 22.1 ($\pm$ 0.9)$\cdot 10^{-15}$ m^2/sec adjacent to the negative electrode.

The Ca content was then measured as a function of distance from the negative electrode in the Ca-doped sample annealed under a field of 300 V/cm for 8 hours. The measured local Ca concentration adjacent to the positive electrode was ***higher*** (19 ± 12 ppm) than that adjacent the negative electrode (10 ± 7 ppm). The high Ca concentration adjacent to the positive electrode infers a low oxygen vacancy concentration, indicating that Ca causes solute-drag and it is the oxygen vacancies at GBs in alumina which increase the GB mobility.

7. Recommendations for Future Work

Disconnection motion is considered to be the main mechanism for GB motion and grain growth. However, the mechanism by which different dopants/impurities, and defects like oxygen vacancies, affect the composition, structure, formation and motion of these disconnections isn't fully understood. To better understand this, disconnections at different GBs should be closely studied using TEM and STEM.

While the inhomogeneous grain growth kinetics due to the application of the electric field suggest that Ca causes solute-drag while oxygen vacancies increase the mobility of GBs, the local concentrations of other dopants like Si and Mg need to be measured. The chemical analyses of excess Ca, Si and Mg at different GBs is also required.

Previous studies have measured the anisotropic GB mobility in alumina by diffusion bonding single crystal sapphire wafers to polycrystalline alumina, performing annealing treatments and measuring the migration distance of the wafer into the polycrystalline region as a function of time. This should be repeated using a perpendicular static electric field to demonstrate the influence of the direction of the field, and a parallel static electric field. Introducing other dopants in alumina, like Mg, is also worth considering.

Considering the influence of the electric field on the local concentrations of dopants/impurities, the field can be used for other types of measurements. For example, a concentration gradient created by the field can be used to then measure the GB diffusion coefficient of different dopants in alumina and other insulating polycrystalline materials.

8. References

1. M. N. Rahaman, *Sintering of Ceramics*, CRC Press, 2008.
2. S. J. L. Lang, *Sintering – Densification, Grain Growth and Microstructure*, Elsevier Butterworth Heinemann, 2005.
3. J. E. Taylor, II – *Mean Curvature and Weighted Mean Curvature*, Acta Metall. Mater., **40**[7]: 1475-1485, 1992.
4. A. Bhattacharya, Y. F. Shen, C. M. Hefferan, S. F. Li, J. Lind, R. M. Suter, C. E. Krill, G. S. Rohrer, *Grain Boundary Velocity and Curvature Are Not Correlated in Ni Polycrystals*, Science, **374**[6564]: 189-193, 2021.
5. V. Muralikrishnan, H. Liu, L.Yang, B. Conry, C. J. Marvel, M. P. Harmer, G. S. Rohrer, M. R. Tonks, R. M. Suter, C. E. Krill III, A. R. Krause, *Observations of Unexpected Grain Boundary Migration in $SrTiO_3$*, Scr. Mater., **222**: 115055, 2024.
6. H. Gleiter, *The mechanism of grain boundary migration*, Acta Metal., **17**: 853-862, 1969.
7. M. G. Lagally, *Atom Motion on Surfaces*, Phys. Today, **46**[11]: 24-31, 1993.
8. J. P. Hirth, R.C. Pond, *Steps, dislocations and disconnections as interface defects relating to structure and phase* transformations, Acta Mater., **44**[12]: 4749-4763, 1996.
9. H. Sternlicht, W. Rheinheimer, M. J. Hoffmann, W. D. Kaplan, *The Mechanism of Grain Boundary Motion in $SrTiO_3$*, J. Mater. Sci., **51**[1]: 467-575, 2016.
10. M. Legros, D. S. Gianola and K. J. Hemker, *In situ TEM observations of fast grain-boundary motion in stressed nanocrystalline aluminum films*, Acta Mater., **56**: 3380-3393, 2008.
11. A. Rajabzadeh, M. Legros, N. Combe, F. Mompiou and D. A. Molodov, *Evidence of grain boundary dislocation step motion associated to shear-coupled grain boundary migration*, Philosophical Magazine, **93**: 1299-1316, 2013.
12. A. Rajabzadeh, F. Mompiou, S. Lartigue-Korinek, N. Combe, M. Legros and D. A. Molodov, *The role of disconnections in deformation-coupled grain boundary migration*, Acta Mater., **77**: 223-235, 2014.
13. T. Radetic, C. Ophus, D. L. Olmsted, M. Asta and U. Dahmen, *Mechanism and dynamics of shrinking island grains in mazed bicrystal thin films of Au*, Acta Mater., **60**: 7051-7063, 2012.
14. N. Combe, F. Mompiou and M. Legros, *Heterogeneous disconnection nucleation mechanisms during grain boundary migration*, Physical Review Materials, **3**: 060601, 2019.
15. J. Han, D. J. Srolovitz, M. Salvalaglio, *Disconnection-Mediated Migration of Interfaces in Microstructures: I. Continuum Model*, Acta Mater., **227**: 117178, 2022.
16. J. D. Powers, A. M. Glaeser, *Grain Boundary Migration in Ceramics*, I. Sci., **6**[1]: 23-39, 1998.

17. J. W. Cahn, *The Impurity-Drag Effect in Grain Boundary Motion*, Acta Metall., **10**[9]: 789-798, 1962.

18. S. J. Dillon, M. P. Harmer, *Relating Grain Boundary Complexion to Grain Boundary Kinetics I: Calcia-Doped Alumina*, J. Am. Ceram. Soc., **91**[7]: 2304-2313, 2008.

19. R. Akiva, A. Berner, W. D. Kaplan, *The Solubility Limit of CaO in α-Alumina at 1600°C*, J. Am. Ceram. Soc., **96**[10]: 3258-3264, 2013.

20. R. Moshe, W. D. Kaplan, *The Influence of CaO on Alumina Grain Boundary Mobility*, J. Eur. Ceram. Soc., **39**[4]: 1324-1328, 2019.

21. S. J. Dillon, M. P. Harmer, *Multiple Grain Boundary Transitions in Ceramics: A Case Study of Alumina*, A. Mater., **55**[15]: 5247-5254, 2007.

22. S. Zamir, *Si Segregation and its Role in Reaching Transparent YAG*, J. Am. Ceram. Soc., **100**[4]: 1689-1696, 2017.

23. M. L. Martin, A. Pundt, R. Kirchheim, *Hydrogen-Induced Accelerated Grain Growth in Vanadium*, Acta Mater., **155**: 262-267, 2018.

24. R. J. Brook, *Pore-Grain Boundary Interactions and Grain Growth*, J. Am. Ceram. Soc., **52**[1]: 56-57, 1969.

25. C. H. Hsueh, A. G. Evans, R. L. Coble, *Microstructure Development During Final/Intermediate Stage Sintering—I. Pore/Grain Boundary Separation*, Acta Metall., **30**[7]: 1269-1279, 1982.

26. I. Levin, D. Brandon, *Metastable Alumina Polymorphs: Crystal Structures and Transition Sequences*, J. Am. Ceram. Soc., **81**[8]: 1995-2012, 1998.

27. M. L. Kronberg, *Plastic Deformation of Single Crystals of Sapphire: Basal Slip and Twinning*, Acta Metall., **5**[9]: 507-524, 1957.

28. D. Brandon, W. D. Kaplan, *Microstructural Characterization of Materials*, John Wiley & Sons, 2013.

29. R. L. Coble, *Transparent Alumina and Method of Preparation*, US Patent Office US3026210A, 1962.

30. S. K Roy, R. L. Coble, *Solubilities of Magnesia, Titania, and Magnesium Titanate in Aluminum Oxide*, J. Am. Ceram. Soc., **5**[1]: 1-6, 1968.

31. S. J. Bennison, and M. P. Harmer, *Effect of MgO Solute on the Kinetics of Grain Growth in $A1_2O_3$*, J. Am. Ceram. Soc., **66**[5]: 90-92,1983.

32. J. Rödel, and A. M. Glaeser, *Anisotropy of Grain Growth in Alumina*, J. Am. Ceram. Soc., **73**[11]: 3292-3301, 1990.

33. L. Miller, A. Avishai, W. D. Kaplan, *Solubility Limit of MgO in Al_2O_3 at 1600°C*, J. Am. Ceram. Soc., **89**[1]: 350-353, 2006.

34. R. Akiva, A. Katsman, W. D. Kaplan, *Anisotropic Grain Boundary Mobility in Undoped and Doped Alumina*, J. Am. Ceram. Soc., **97**[5]: 1610-1618, 2014.

35. S. Baik, J. H. Moon, *Effects of Magnesium Oxide on Grain-Boundary Segregation of Calcium During Sintering of Alumina*, J. Am. Ceram. Soc., **74**[4]: 819-822, 1991.

36. S. I. Bae, and S. Baik, *Determination of Critical Concentrations of Silica and/or Calcia for Abnormal Grain Growth in Alumina*, J. Am. Ceram. Soc., **76**[4]: 1065-1067, 1993.

37. J. Jung, S. Baik, *Abnormal Grain Growth of Alumina: CaO Effect*, J. Am. Ceram. Soc., **86**[4]: 644-649, 2003.

38. A. Altay, M. A. Gülgün, *Microstructural Evolution of Calcium-Doped α-Alumina*, J. Am. Ceram. Soc., **86**[4]: 623-629, 2003.

39. P. Ghosh, R. Marder, A. Berner, W. D. Kaplan, *The Influence of Temperature on the Solubility Limit of Ca in Alumina*, J. Eur. Ceram. Soc., **40**[15]: 5767-5772, 2020.

40. I. J. Bae, S. Baik, *Abnormal Grain Growth of Alumina*, J. Am. Ceram. Soc., **[80]**5: 1149-1156, 1997.

41. S. J. Dillon, M. P. Harmer, *Relating Grain Boundary Complexion to Grain Boundary Kinetics II: Silica-Doped Alumina*, J. Am. Ceram. Soc., **91**[7]: 2314-2320, 2008.

42. R. Moshe, A. Berner, W. D. Kaplan, *The Solubility Limit of SiO_2 in α-alumina at 1600°C*, Scr. Mater., **39**[4]: 1324-1328, 2014.

43. Z. A. Munir, U. Anselmi-Tamburini, M. Ohyanagi, *The Effect of Electric Field and Pressure on the Synthesis and Consolidation of Materials: A Review of the Spark Plasma Sintering Method*, J. Mater. Sci., **41**[3]: 763-777, 2006.

44. J. R. Groza, *Field Activation Provides Improved Sintering*, Met. Powder Rep., **7**[55]: 16-18, 2000.

45. Z. Shen, M. Johnsson, Z. Zhao, M. Nygren, *Spark Plasma Sintering of Alumina*, J. Am. Ceram. Soc., **85**[8]: 1921-1927, 2002.

46. B. N. Kim, K. Hiraga, K. Morita, H. Yoshida, *Spark Plasma Sintering of Transparent Alumina*, Scr. Mater., **57**[7]: 607-610, 2007.

47. D. Chakravarty, S. Bysakh, K. Muraleedharan, T. N. Rao, R. Sundaresan, *Spark Plasma Sintering of Magnesia-Doped Alumina with High Hardness and Fracture Toughness*, J. Am. Ceram. Soc., **91**[1]: 203-208, 2008.

48. M. Biesuz, V. M. Sglavo, *Flash Sintering of Ceramics*, J. Eur. Ceram. Soc., **39**[2]: 115-143, 2019.

49. M. Cologna, J. S. C. Francis, R. Raj, *Field Assisted and Flash Sintering of Alumina and its Relationship to Conductivity and MgO-Doping*, J. Eur. Ceram. Soc., **31**[15]: 2827-2837, 2011.

50. M. Biesuz, V. M. Sglavo, *Flash Sintering of Alumina: Effect of Different Operating Conditions on Densification*, J. Eur. Ceram. Soc., **36**[10]: 2535-2542, 2016.

51. R. Marder, A. Karlin, G. Shter, G. Grader, W. D. Kaplan, *The Influence of Electric Fields on Grain Boundary Mobility in Alumina*, J. Eur. Ceram. Soc., **45**[4]: 117069, 2025.

52. J. W. Jeong, J.H. Han, D. Y. Kim, *Effect of Electric Field on the Migration of GBs in Alumina*, J. Am. Ceram. Soc., **83**[4]: 915-918, 2000.

53. W. Rheinheimer, M. Fulling, M. J. Hoffmann, *Grain Growth in Weak Electric Fields in Strontium Titanate: Grain Growth Acceleration by Defect Redistribution*, J. Eur. Ceram. Soc., **36**[11]: 2773-2780, 2016.

54. W. Rheinheimer, J. P. Parras, J.-H. Preusker, R. A. De Souza, M. J. Hoffmann, *Grain Growth in Strontium Titanate in Electric Fields: The Impact of Space-Charge on the Grain Boundary Mobility*, J. Am. Ceram. Soc., **102**[6]: 3779-3990, 2019.

55. L. A. Hughes, M. Marple, K. Van Benthem, *Electrostatic Fields Control Grain Boundary Structure in $SrTiO_3$*, Appl. Phys. Lett., **113**[4]: 041604, 2018.

56. L. A. Hughes, K. Van Benthem, *Effects of Electrostatic Field Strength on Grain-Boundary Core Structures in $SrTiO_3$*, J. Am. Ceram. Soc., **102**[8]: 4502-4510, 2019.

57. W. Qin, D. N. F. Muche, R. H. R. Castro, K. Van Benthem, *The Effect of Electric Fields on Grain Growth in $MgAl_2O_4$ Spinel*, J. Eur. Ceram. Soc., **38**[16]: 5512-5518, 2018.

58. https://products.sasol.com/pic/products/home/grades/ZA/5ceralox/index.html, last visited on July 3rd, 2025.

59. https://www.carloerbareagents.com/cerstorefront/cer-it/, last visited on July 3rd, 2025.

60. https://www.col-int.com/products/conductive-platinum-paste-ink?variant=42300837822689, last visited on July 3rd, 2025.

61. https://buyplatinumwire.com/, last visited on July 3rd, 2025.

62. https://gavish.com/custom-fabricated-sapphire/, last visited on July 3rd, 2025.

63. J. I. Goldstein, D. E. Newbury, J. R. Michael, N. W. M. Ritchie, J. H. J. Scott, D. C. Joy, *Scanning Electron Microscopy and X-Ray Microanalysis*, Springer New York, 2018

64. M. I. Mendelson, *Average Grain Size in Polycrystalline Ceramics*, J. Am. Ceram. Soc., **52**[8]: 443-446, 1969.

65. A. Berner, F. Gimelfarb, T. Ukhorskaya, *Metrological Aspects of Microprobe Analysis*, J. Anal. Chem., **37**[2]: 338–348, 1982.

66. R. Moshe, W. D. Kaplan, *The Combined Influence of Mg and Ca on Microstructural Evolution of Alumina*, J. Am. Ceram. Soc., **102**[8]: 4882-4887, 2019.

67. J. Han, S. L. Thomas, D. J. Srolovitz, *Grain-boundary kinetics: A unified approach*, Prog. Mater. Sci., **98**: 386-476, 2018.

68. R. W. Grimes, *Solution of MgO, CaO, and TiO_2 in α-Al_2O_3*, J. Am. Ceram. Soc., **77**[2]: 378-384, 1994.

69. K. P. D. Lagerlöf and R. W. Grimes, *The defect chemistry of sapphire (α-Al_2O_3)*), Acta Mater., **46**[16]: 5689-5700, 1998.

70. K. J. W. Atkinson, R. W. Grimes, M. R. Levy, Z. L. Coull, T. English, *Accommodation of Impurities in α-Al_2O_3, α-Cr_2O_3 and α-Fe_2O*, J. Eur. Ceram. Soc., **23**[16]: 3059-3070, 2003.

71. R. Marder, P. Ghosh, I. Reimanis, W. D. Kaplan, *The Influence of Carbon on the Microstructure and Wear Resistance of Alumina*, J. Am. Ceram. Soc., **104**[8]: 4214-4225, 2021.

72. B. Qu, D. Eiteneer, L. A. Hughes, J. H. Preusker, J. Wood, W. Rheinheimer, M. J. Hoffmann, K. Van Benthem, *Defect Redistribution Along GBs in $SrTiO_3$ by Externally Applied Electric Fields*, J. Eur. Ceram. Soc., **43**[2]: 1625-1632, 2023.

השפעת שדות חשמליים על התפתחות המיקרומבנה של אלומינה

אסף ראובן קזמירסקי

השפעת שדות חשמליים על התפתחות המיקרומבנה של אלומינה

חיבור על מחקר

לשם מילוי חלקי של הדרישות לקבלת התואר

מגיסטר למדעים בהנדסת חומרים

אסף ראובן קזמירסקי

הוגש לסנט הטכניון – מכון טכנולוגי לישראל

אב תשפ"ה חיפה יולי 2025

המחקר הזה נערך בהנחיית **פרופ' וויין ד. קפלן** מהפקולטה למדע והנדסה של חומרים בטכניון – מכון טכנולוגי לישראל.

אני מודה לקרן הלאומית למדע (ISF 544/22) על התמיכה הכספית הנדיבה בהשתלמותי.

תקציר

גידול גרעינים הוא תהליך שמתרחש בו־זמנית עם ציפוף (densification) במהלך סִנטור של חומרים קרמיים. גודל הגרעינים ושטח גבולות הגרעין משחקים תפקיד מרכזי בקביעת התכונות המכניות והפונקציונליות של חומרים רב גבישיים. לכן, הבנה מעמיקה של תהליך גידול הגרעינים היא חיונית לשליטה והנדוס של תכונות החומר הקרמי.

אחת מהמערכות הקרמיות הנחקרות ביותר היא אלפא-אלומינה (α-Al_2O_3), הנפוצה בשימושים תעשייתיים רבים. מחקרים רבים הראו כי תוספים (dopants) ו/או זיהומים באלומינה עשויים לגרום לשינויים משמעותיים בקינטיקה של גידול הגרעינים, דבר שמשפיע באופן ישיר על המיקרו-מבנה הסופי והתכונות של החומר. לדוגמה, הוכח כי תוספת של סידן (Ca) בריכוז נמוך מתחת לסף המסיסות שלו באלומינה מובילה לניידות גבולות גרעין מואצת ואנאיזוטרופית, אשר יוצרת גרעינים מוארכים.

כמו כן, הוכח כי שדות חשמליים – הנמצאים בשימוש בטכניקות סִנטור כמו Spark Plasma Sintering (SPS) ו- Flash sintering – משפיעים גם הם על קצב גידול הגרעינים. באלומינה, ההסבר הנפוץ לתופעה הוא המשיכה של היעדרויות חמצן בעלות מטען חשמלי מקומי חיובי אל האלקטרודה השלילית. תוספת של סידן לאלומינה מגבירה את כמות היעדרויות החמצן המצויות באלומינה על מנת לפצות על הפרש המטען בין יוני הסידן לבין יוני האלומיניום.

מטרת המחקר הנוכחי הייתה להבין את ההשפעה של סידן ושדה חשמלי סטטי על גידול גרעינים באלומינה, הן באלומינה לא מסוממת והן באלומינה עם תוספת סידן (6 ו-19 חלקים למיליון – ppm – בהתאמה) על ידי מדידת הניידות האפקטיבית של גבולות הגרעין עם ובלי שדה חשמלי חיצוני. המחקר שאף לאשש את ההשפעה של השדה החשמלי על תהליך גידול הגרעינים.

הפעלת השדה החשמלי נעשית במטרה להפריד בין יוני הסידן לבין היעדרויות החמצן שמאזנות את מטענם, ובכך לחקור את ההשפעה של ריכוזי תוספים, זיהומים מקומיים ופגמים קריסטלוגרפיים על גידול הגרעינים. גישה זו מאפשרת להבין טוב יותר את האינטראקציה בין רכיבים טעונים והשפעתה על מבנה הגרעינים.

לפני תהליך החישול, האלומינה עברה סִנטור באוויר בטמפרטורה של 1600°C למשך שעתיים. לאחר מכן, הדגמים עברו חישול באוויר באותה טמפרטורה למשכי זמן של 2, 4, 6 ו-8 שעות עם וללא הפעלת שדה חשמלי.

במהלך הטיפולים התרמיים, דגמי אלומינה לא מסוממת ודגמים עם תוספת סידן הונחו בין שתי אלקטרודות בתוך תנור צינורי, ועברו חישול עם וללא שדה חשמלי. על סמך מדידות של גודל גרעין ממוצע כתלות בזמן, הניידות האפקטיבית של גבולות הגרעין חושבה.

נמצא כי העלאת ריכוז הסידן מעלה את הניידות האפקטיבית של גבולות הגרעין מ־11.3×10^{-15} מ"ר לשנייה באלומינה לא מסוממת ל-22.9×10^{-15} מ"ר לשנייה באלומינה עם סידן. כאשר הופעל שדה חשמלי בעוצמה של 200 וולט לס"מ על דגמי האלומינה הלא מסוממת, נמדדו הערכים הבאים:

4.9×10^{-15} מ"ר לשנייה ליד האלקטרודה החיובית.
10.1×10^{-15} מ"ר לשנייה במרכז הדגם,
9.1×10^{-15} מ"ר לשנייה ליד האלקטרודה השלילית.

כאשר עוצמת השדה עלתה ל-300 וולט לס"מ, התקבלו הערכים:

5.0×10^{-15} מ"ר לשנייה ליד האלקטרודה החיובית,
8.3×10^{-15} מ"ר לשנייה במרכז הדגם,
12.0×10^{-15} מ"ר לשנייה ליד האלקטרודה השלילית.

עבור דגמי האלומינה עם תוספת הסידן, אשר עברו חישול תחת שדה של 300 וולט לס"מ, התקבלו ערכי הניידות:

8.5×10^{-15} מ"ר לשנייה ליד האלקטרודה החיובית,
14.3×10^{-15} מ"ר לשנייה במרכז הדגם,
22.1×10^{-15} מ"ר לשנייה ליד האלקטרודה השלילית.

על מנת להבין את פרופיל ההתפלגות של הסידן תחת השפעת השדה החשמלי, בוצעה אנליזה כמותית באמצעות ספקטרוסקופיית פיזור אורך גל (Wavelength dispersive spectroscopy - WDS). האנליזה בוצעה על דגם שעבר חישול של 8 שעות תחת השדה החשמלי, ונמצא כי השדה גורם להתפלגות לא אחידה של סידן לאורך הדגם – ככל שמתרחקים מהאלקטרודה השלילית, ריכוז הסידן עולה.

ערכי הניידות שנמדדו **תאמו באופן הפוך** להתפלגות זו: באזור שבו ריכוז הסידן המקומי היה גבוה יותר (19 ppm), ליד האלקטרודה החיובית, נמדדה ניידות נמוכה יותר. באזור שבו ריכוז הסידן המקומי היה נמוך יותר, (10 ppm), ליד האלקטרודה השלילית, נמדדה ניידות גבוהה יותר. ממצאים אלה מחזקים את

ההשערה שהיעדרויות החמצן הן שאחראיות להאצת תנועת גבולות הגרעין, בעוד שיוני הסידן לבדם גורמים לאפקט הידוע בתור (solute-drag), אשר מאט את תנועת גבולות הגרעין.